Received: 31 May 2023 | Revised: 2 April 2024 | Accepted: 8 April 2024

DOI: 10.1002/eqe.4131

RESEARCH ARTICLE

WILEY

Pseudo-dynamic testing, repairability, and resilience assessment of a large-scale steel structure equipped with self-centering column bases

Elena Elettore[1] | **Fabio Freddi**[2] | **Massimo Latour**[1] | **Vincenzo Piluso**[1] | **Gianvittorio Rizzano**[1]

[1]Department of Civil Engineering, University of Salerno, Salerno, Italy

[2]Department of Civil, Environmental and Geomatic Engineering, University College London, London, UK

Correspondence
Fabio Freddi, Department of Civil, Environmental and Geomatic Engineering, University College London, London, UK.
Email: f.freddi@ucl.ac.uk

Abstract

Recent destructive seismic events have underlined the need for increasing research efforts devoted to the development of innovative seismic-resilient structures able to reduce seismic-induced direct and indirect losses. Regarding steel Moment Resisting Frames (MRFs), the inclusion of Friction Devices (FDs) in Beam-to-Column Joints (BCJs) has emerged as an effective solution to dissipate the seismic input energy while ensuring a damage-free behavior. Additionally, recent studies have demonstrated the benefits of implementing similar damage-free solutions for Column Bases (CBs). In this context, the authors have recently experimentally investigated a Self-Centering CB (SC-CB) aimed at residual drift reduction. Previous experimental tests only focused on the response of isolated SC-CBs under cyclic loads. Conversely, the present paper advances the research through an experimental campaign on a large-scale steel structure equipped with the proposed SC-CBs, providing valuable insights into the global structural response and improved repairability. A set of eight Pseudo-Dynamic (PsD) tests were conducted considering different records and configurations of the structure. The experimental results highlighted the effectiveness of the SC-CBs in minimizing the residual interstory drifts and protecting the first-story columns from damage, thus enhancing the structure's resilience. Moreover, the consecutive PsD tests allowed investigating the effectiveness of the reparation process in restoring the seismic performance of the 'undamaged' structure. An advanced numerical model was developed in OpenSees and validated against the global and component-level experimental results. Incremental Dynamic Analyses were finally performed to investigate the influence of the SC-CBs on the structure's seismic response while accounting for the record-to-record variability.

KEYWORDS

large-scale structure, pseudo-dynamic tests, repairability, residual drifts, resilience, self-centering column bases

1 | INTRODUCTION

Steel Moment Resisting Frames (MRFs) are widely used seismic-resistant systems for building structures.[1,2] For these structures, the traditional seismic design philosophy, suggested by seismic codes and guidelines,[3–5] relies on the inelastic deformations of structural components (i.e., damage) to dissipate the seismic input energy. This often leads to post-earthquake scenarios where the building structure is significantly damaged, difficult to repair, or in need of demolition/reconstruction, involving considerable direct (i.e., repair costs) and indirect (i.e., downtime) losses, which are not acceptable from both the social and economic perspectives.[6,7] To avoid such inconveniences, nowadays' earthquake engineering is directing a growing research effort to develop seismic-resilient structures to reflect performance goals in terms of post-earthquake reoccupancy and functional recovery time.[8–13]

Regarding steel MRFs, the use of Friction Devices (FDs) in Beam-to-Column Joints (BCJs)[14–16] has been recently widely investigated as a promising strategy to provide both high local ductility and energy dissipation capacity with only minor yielding and wearing within replaceable elements.[17–22] However, although the use of FDs represents an efficient strategy to protect the BCJs' components from local damage, global damage can still be observed in the form of significant postearthquake residual drifts[23,24] which can exceed the commonly accepted reparability limits suggested by FEMA P58-1[25] (i.e., residual drifts < 0.5% for cases where repairability is economically convenient or <0.2% for cases where no structural realignment is necessary). This issue has been tackled by several research works introducing elastic restoring forces able to regulate the structure's Self-Centering (SC) capability by including high-strength Post-Tensioned (PT) steel bars or strands combined with replaceable dissipative devices to control gap-opening (i.e., rocking) mechanisms at the BCJs.[26–29]

Besides, it has also been demonstrated that protecting the Column Bases (CBs) is paramount to achieve structural resilience.[30,31] Several CB configurations exist and are usually classified according to their interaction with the reinforced concrete foundation, such as embedded,[32] shallowly embedded,[33] concrete-encased,[34] or exposed.[35,36] However, conventional full- or partial-strength CBs are characterized by significant drawbacks. Conventional full-strength steel CBs may suffer from local buckling,[37] axial shortening phenomena,[38] and large plastic deformations,[39] which may impair structure repairability after severe earthquakes. Conversely, the design of partial-strength steel CBs needs the knowledge of their complex hysteretic behavior under cyclic loadings, which is difficult to predict,[35,36] and hence this strategy is rarely followed.

To address these issues, several novel CB configurations have been proposed in the last few decades, having the advantage of providing enhanced performance under cyclic loadings.[40–50] Some strategies focused on replacing the conventional full-strength CB connections with dissipative partial-strength joints equipped with energy dissipation devices (e.g., yielding or FDs)[40,41] or with a combination of such devices and SC systems.[42–46] For example, Freddi et al.[42] proposed and experimentally investigated[43] a damage-free steel CB using high-strength PT bars and FDs and a circular plate with rounded edges as a rocking base. Wang et al.[45] experimentally and numerically examined two types of SC-CBs composed of a concrete-filled square steel section, showing stable SC and energy dissipation capabilities. Additionally, other innovative CB solutions were based on promoting dissipative mechanisms[47,48] (e.g., anchor rod yielding[47]). For example, Inamasu et al.[48] recently tested a large-scale novel dissipative embedded CBs, demonstrating the advantages of preventing local buckling-induced axial shortening while dissipating the energy within a predefined zone.

In this context, Latour *et al.*[50] proposed and experimentally studied a novel SC-CB consisting of a rocking column splice joint where a combination of FDs and PT bars with Disk Springs (DSs) are, respectively, used to dissipate the seismic energy and promote the SC behavior of the connection. Component tests of an isolated SC-CB specimen subjected to cyclic loads demonstrated a good and stable flag-shaped hysteretic behavior, with negligible residual deformations in the column. Concerning this connection typology, the authors have recently carried out extensive numerical simulations to evaluate the effectiveness of these joints in reducing the residual drifts within several case-study steel MRFs.[51,52] Moreover, additional research studies investigated the relevant design parameters affecting the local behavior of the SC-CBs, such as the design axial load, the shear distribution among the components, as well as the key role of the post-tensioning force of the PT bars in controlling the SC response.[54]

Although the aforementioned research studies demonstrated the feasibility of the SC-CBs and significantly contributed to defining design strategies for the proposed technology, further research is needed to experimentally assess the global response of large-scale case-study structures equipped with this connection typology. In addition, while many tests of isolated innovative CBs are currently available,[41,43,45,47] the influence of the local behavior of such connections on the overall response of MRFs under seismic loading conditions has rarely been experimentally analyzed.[55] In addition, experimental tests are also essential to evaluate and test the repairability of the structure. In this direction, a few research studies

focused on innovative structural solutions that can be easily and quickly repaired in the aftermath of an earthquake.[56,57] For example, Zhang *et al.*[57] investigated simple repairing techniques (i.e., retightening the bolts of the FDs) for a novel steel rocking CB joint with FDs to restore the initial performance without losing strength and stiffness. However, experimental evidence on suitable structural restoring techniques for structural performance recovery is still limited. Consequently, the overall lack of confidence in the future behavior of repaired structures can represent a relevant factor contributing to the high demolition rates. These considerations motivated the current research activity, whose main objectives are: (i) to experimentally assess the influence of SC-CBs on the overall structural performance of a large-scale steel structure; (ii) to collect data for modeling validation; and (iii) to provide further investigations regarding the structure's repairability and seismic resilience.

To fulfill these objectives, this paper presents an experimental program comprising several Pseudo-Dynamic (PsD) tests[58] conducted on a large-scale two-story steel structure equipped with Damage-Free BCJs (DF-BCJs) endowed with FDs and SC-CB connections. The experimental campaign has been performed at the STRENGTH Laboratory of the University of Salerno, Italy. The test specimen is first described, including a presentation of the characterization tests for materials and components. Then, the experimental program is shown, including the test matrix, the experimental setup, and the instrumentations. Preliminary white-noise tests with low-intensity earthquakes were conducted to evaluate the dynamic response of the structures in the elastic range. A sequence of eight high-intensity ground motion records was successfully applied to assess the seismic response. Global and local Engineering Demand Parameters (EDPs) have been monitored to investigate the influence of the proposed SC-CBs on the seismic performance of the tested structure. Results demonstrated the effectiveness of the SC-CBs in limiting the residual drifts below the acceptable limits.[24] Additionally, at the end of each test, the specimen has been repaired by loosening and retightening the high-strength bolts belonging to the FDs of both DF-BCJs and SC-CBs. Similar operations were performed on the PT bars. The repairing process highlighted the key role of the SC-CBs in the residual drift recovery, representing a considerable benefit in terms of resilience,[59] repairability,[60] and functional recovery.[61] Similarly, the consecutive PsD tests allowed investigating the effectiveness of the reparation process in restoring the seismic performance of the 'undamaged' structure. A detailed Finite Element (FE) model was developed in OpenSees,[62] and comparisons between experimental and numerical results are presented for two ground motion records, discussing the accuracy and limitations of the modeling strategy. Finally, Incremental Dynamic Analyses (IDAs)[63] were performed to numerically investigate the PT bars' influence on the structure's seismic response while also considering the influence of record-to-record variability.

This paper is organized as follows: Section 2 describes the experimental program, including the description and design of the specimen, the design methodology and performance objectives, the material properties, the test setup, and the instrumentations; Section 3 presents the results of the experimental campaign; Section 4 validates the FE model against the experimental results; while Section 5 discusses the performance of the structure in terms of repairability and resilience.

2 | EXPERIMENTAL PROGRAM

2.1 | Description and design of the test specimen

The test specimen is a large scale (i.e., 75%) representation of a prototype structure characterized by two stories and three bays in both directions. The reference structure is part of a wider experimental campaign and is described in detail by Di Benedetto *et al.*,[23] who experimentally investigated the same specimen equipped only with DF-BCJs. Table 1 reports the indications of the design values of the dead (G_k) and live (Q_k) loads and masses of the prototype structure for each MRF, whose tributary area corresponds to 25% of the total floor area (i.e., the building includes four seismic-resisting MRFs in both directions). Figure 1 shows the plan and elevation views of the test specimen. The interstory heights are equal to 2.40 m at both stories, while the longitudinal and transversal bays have span lengths equal to 4 and 2 m. The specimen is characterized by two longitudinal MRFs and two transversal bracings to prevent undesired accidental torsional effects.

TABLE 1 Loads and masses for each Moment Resisting Frame (MRF).

Level [–]	G_k [kN/m^2]	Q_k [kN/m^2]	Mass [tons]
First level	3.90	3.60	19.00
Second level	3.00	0.50	14.20

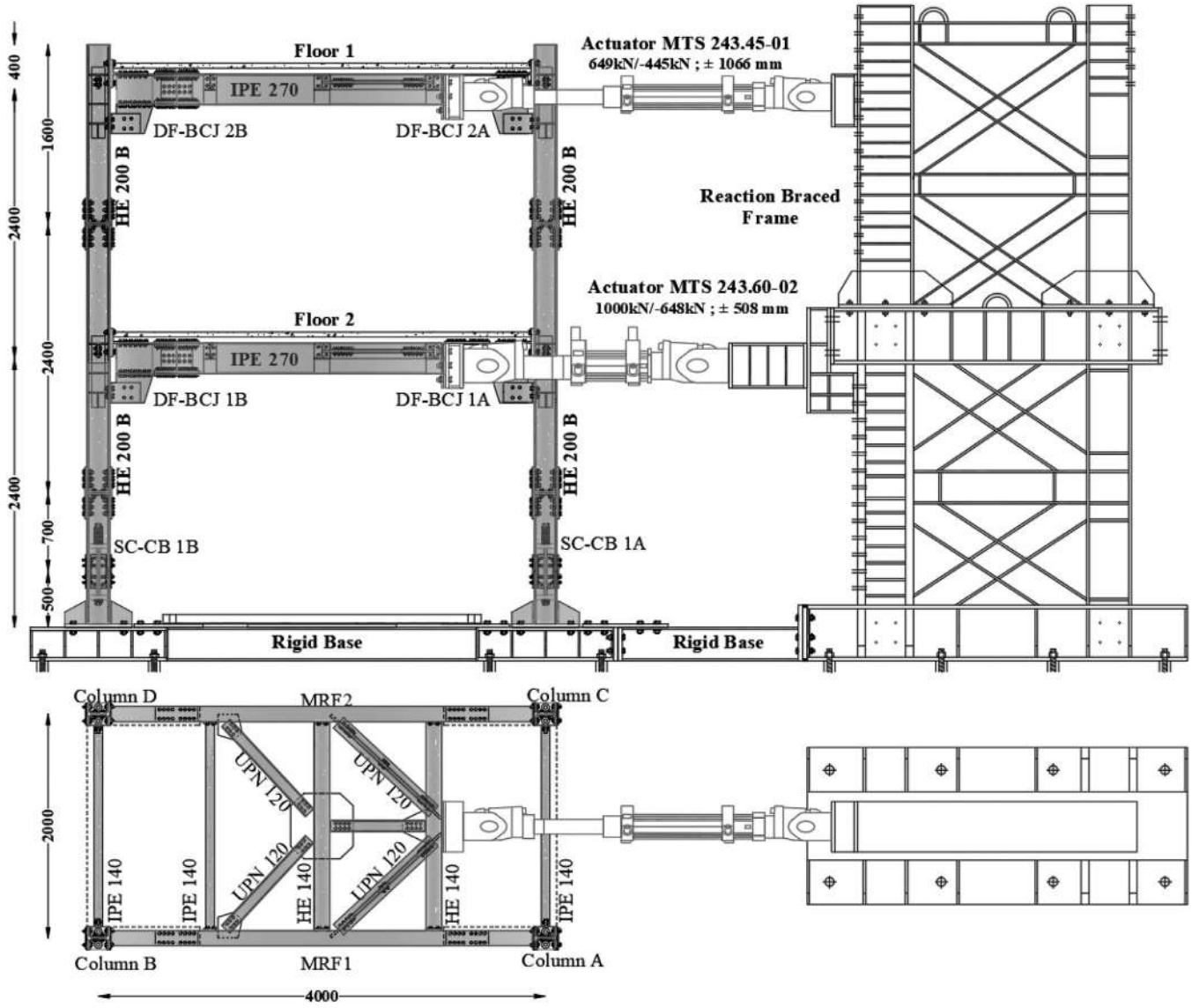

FIGURE 1 Plan and elevation view of the test specimen.

The floor system is formed by a HI BOND A55/P600 steel-concrete composite floor with a total height equal to 100 mm, and five equally spaced IPE 140 and HE 140B secondary beams connected to the concrete slab with shear studs, while UPN 120 are used as in-plane bracings. The design is carried out following the Eurocode (EC) 8 provisions.[3] The design earthquake at the Ultimate Limit State (i.e., ULS: probability of exceedance of 10% in 50 years) is defined considering the Type 1 elastic response spectrum with a PGA equal to 0.35 g, soil type B, and an importance factor equal to 1. The Collapse Limit State (i.e., CLS, probability of exceedance of 2% in 50 years) is assumed to have an intensity equal to 150% of the ULS.[5] The MRF is characterized by plan and elevation regularity. The mass of each story is evaluated based on the seismic combination of the EC 8.[3] The behavior factor is defined according to EC 8[3] requirements for MRFs in DCH and hence assumed as $q = 6$. The interstory drift limit for the Damage Limit State (i.e., DLS: probability of exceedance of 10% in 10 years) is assumed to be 1%[3] for nonstructural elements fixed in a way such as not to interfere with structural deformations. The beams and columns are designed and checked to comply with EC 8 requirements,[3] and their cross-sections are, respectively, IPE 270 and HE 200B, with steel grade S355. It is highlighted that the stiffness requirement related to the DLS controls the sizing of beams and columns. The P-delta effects are considered negligible as the interstory drift sensitivity coefficient θ is lower than 0.1 at both stories.[3] The slab is disconnected from the nodal region by leaving an appropriate gap between the concrete slab and the columns, consistently with the EC 8[3] provisions. The two MRFs are equipped with DF-BCJs and SC-CB connections, whose design is detailed in Sections 2.1.1 and 2.1.2.

The design criteria described in this and the following sections aim at meeting the following performance objectives: (i) interstory drifts not exceeding 1% for the DLS seismic intensity; (ii) joint rotations for DF-BCJs and SC-CBs not exceeding the limit set by EC 8[3] provisions; (iii) negligible structural damage up to the CLS seismic intensity with energy dissipation only provided by the sliding mechanism in the FDs of the DF-BCJs and SC-CBs; (iv) limited residual drifts resulting from the complete SC response of the SC-CBs; and (v) easy and quick repairability of the structure and performance of the repaired structure comparable with the original one.

2.1.1 | Damage-Free Beam-to-Column Joints (DF-BCJs)

Figure 2(A) shows the DF-BCJ[17–22] adopted in this experimental campaign and also tested by Di Benedetto *et al.*[23] In this configuration, the FD is constituted by a steel haunch bolted to the bottom beam flange and two steel L-stubs bolted to the column's flange and the haunch. The friction pads are symmetrically placed between the L-stubs and the haunch. These elements are clamped together with high-strength bolts, which are used to tune the friction force in the FDs. The top beam flange is bolted to the column's flange with a steel T-stub, fixing the Centre of Rotation (COR).

Figure 2(B) shows the DF-BCJ's deformed configuration and design actions. The design methodology is based on a step-by-step procedure consisting of: (i) definition of the design input parameters; (ii) design of the dissipative components; and (iii) design of the nondissipative components. Additional information regarding the design procedure is provided in Francavilla *et al.*[21] The proposed design procedure starts from the identification of the bending moments acting in the joints and corresponding to the different limit states (i.e., $M_{Ed,DLS}$ is the bending moment at the DLS, corresponding to the 'no-slippage' design condition; $M_{Ed,ULS}$ is the bending moment at the ULS, corresponding to the 'slippage' design condition). Starting from the design slippage force (i.e., $F_{slip,d}$, defined as $M_{Ed,ULS}$ divided by the lever arm z), the number of bolts and their preload forces are defined. It is highlighted that $F_{slip,d}$ depends only on the moment demand, and the moment-shear interaction is negligible, as demonstrated by previous research studies.[19,20] Subsequently, once the FD is geometrically defined, all the remaining non-dissipative components (e.g., T-stub and L-stub) are designed to be sufficiently over-resistant by applying a proper overstrength factor. The resulting forces are identified in Figure 2(B) and correspond to shear and tension forces (i.e., $V_{nd,d}$ and $F_{nd,d}$) for the T-stub and a tension force (i.e., $F_{nd,d}$) for the L-stubs. The overstrength factor, assumed equal to 1.83[19] in the present study, amplifies the design actions to account for the random variability of the bolt installation preload and friction coefficient. Finally, to assure a sufficient rotational supply, the length of the horizontal slots of the FD is designed to accommodate a rotation of 0.035 rads, as conventionally assumed according to EC 8,[3] plus a tolerance of 0.01 rads. It is highlighted that the strength design of the DF-BCJ also considers the minimum partial strength ratio required by the current revision of the EC 8.[65] Table 2 summarizes the design input and FDs' main geometrical and structural properties. The FDs comprise 8 mm friction pads made of S355 steel plates coated with a thermally sprayed material. The friction coefficient (μ) has been experimentally evaluated, as reported in

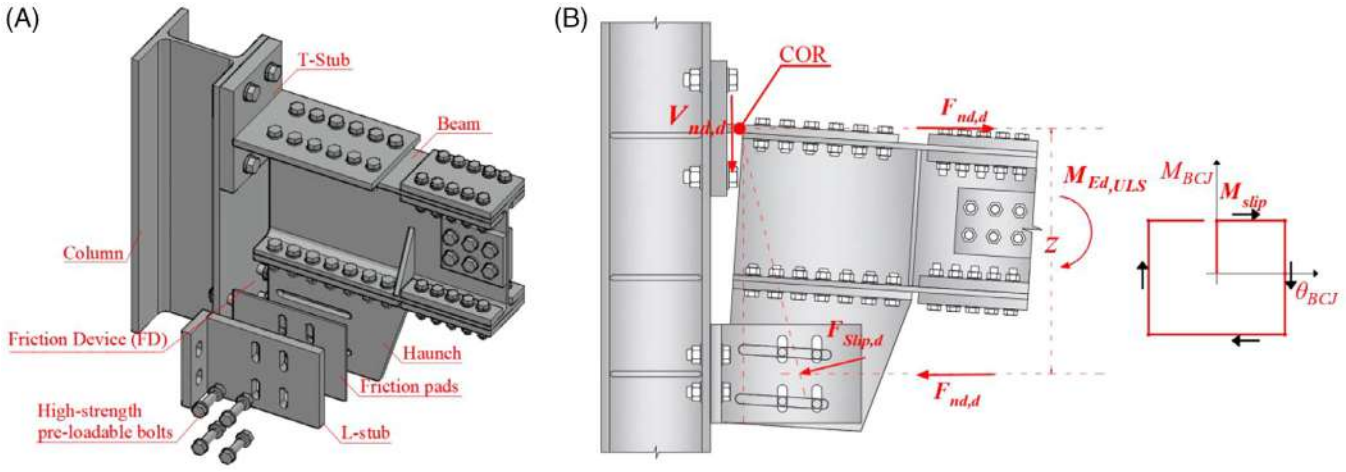

FIGURE 2 Damage-Free Beam-to-Column Joint (DF-BCJ): (A) Geometrical configuration; (B) Deformed configuration, design actions, and theoretical hysteretic behavior.

TABLE 2 Damage-Free Beam-to-Column Joint (DF-BCJ): Design input, geometry, and structural properties.

z [m]	$M_{Ed,ULS}$ [kNm]	$F_{slip,d}$ [kN]	n_b [–]	n_s [–]	Class [–]	d [mm]	Preload [kN]	Torque [Nm]	slot [mm]
0.400	103	234	4	2	HV 10.9	M16	55	145	170

Section 2.2. It is noteworthy that the design tightening torque is amplified by a partial safety factor of 1.10 to compensate for short-term preload losses.[22]

2.1.2 | Self-Centering Column Bases (SC-CBs)

Figure 3(A) shows the SC-CBs of this experimental campaign. They consist of a column composed of two parts connected by a combination of FDs on both web and flanges to dissipate the seismic input energy, and a SC system. Similarly to the DF-BCJs, the FDs consist of friction pads and cover plates clamped with high-strength bolts on both web and flanges. The SC system is composed of high-strength PT bars symmetrically placed and assembled in series with a system of DSs.

Figure 3(B) shows the forces developed during the gap-opening phase. The FDs are assumed to exhibit a rigid-plastic behavior. The design slippage force of web ($F_{w,slip,d}$) and flanges ($F_{f,slip,d}$) FDs depends on the design value of the friction coefficient (μ), number of bolts and friction interfaces, and preloading forces of each web and flange bolt, respectively. The SC-CB is characterized by a flag-shaped moment-rotation behavior. The moments' contributions are a function of the forces developed by each component during the gap-opening phase and can be calculated with respect to the COR located at the center of the column's flange. The four fundamental moments defining the entire cyclic moment-rotation behavior (i.e., M_1, M_2, M_3, and M_4) are reported in Figure 3(C), where M_1 is the moment at the onset of rocking, while M_2 is the maximum moment achieved at the target rotation θ_t.

The objective of the design procedure is to satisfy at the same time three main conditions: (i) no yielding of the column; (ii) SC behavior (i.e., decompression moment higher than the moment contribution of the friction devices); and (iii) bending moment corresponding to the gap opening (M_1) higher than the one defined by EC 8[3] for the seismic design combination according to the ULS ($M_{Ed,ULS}$). The design of the SC-CB is based on a step-by-step procedure consisting of: (i) definition of the design input parameters; (ii) design of the dissipative and SC components; and (iii) design of the non-dissipative components. Additional information about the design procedure and the key assumptions can be found in

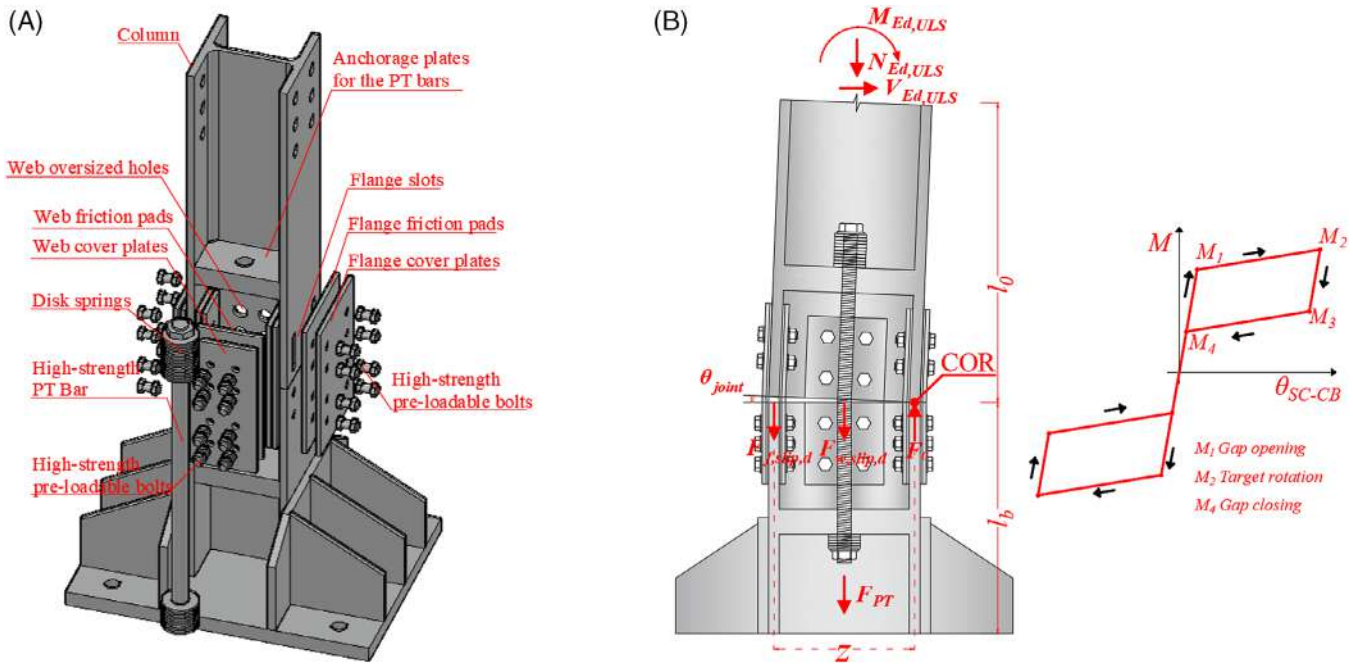

FIGURE 3 Self-Centering Column Base (SC-CB): (A) Geometrical configuration; (B) Deformed configuration and theoretical hysteretic behavior.

TABLE 3 Self-Centering Column Base (SC-CB) design input.

Profile [–]	Splice (l_b) [mm]	z [mm]	$M_{Ed,ULS}$ [kNm]	$N_{Ed,ULS}$ [kN]	$V_{Ed,ULS}$ [kN]
HE 200B	500	185	127	+138, −127	115

Note: Negative values are for tension; positive values are for compression.

TABLE 4 Self-Centering Column Base (SC-CB) geometrical and structural properties.

Element [–]	n_b [–]	Class [–]	d [mm]	Preload [kN]	Torque [Nm]
Web bolts	4	HV 10.9	M14	28	65
Flange bolts	4	HV 10.9	M14	26	60
PT bars	2	10.9	M30	400	1000
DSs	3 n_{par}, 8 n_{ser}	C60S	D30	–	–

previous works.[51–54] The design input parameters are: (i) the geometrical properties of the column (i.e., cross-section properties and splice position above the foundation—l_b); and (ii) the design forces in the column (i.e., maximum/minimum expected axial forces—$N_{Ed,ULS,min}$, $N_{Ed,ULS,max}$—and bending moment—$M_{Ed,ULS}$) derived through the procedure suggested by EC 8.[3] The design procedure assumes that the web FDs carry the design shear load ($V_{Ed,ULS}$) alone. Additional considerations about the transfer mechanism of shear forces in the components of the SC-CBs are detailed in Elettore *et al.*[54]

Once the input parameters are selected, the SC-CB is designed by first sizing the bolts of the web FD and, successively, the PT bars and the bolts of the flanges FDs. PT bars are designed to remain elastic to ensure the structure's SC response up to the design rotation. The yielding of the PT bars is avoided by installing a proper number of DSs arranged in series (n_{ser}) and parallel (n_{par}), granting an adaptable stiffness–resistance combination to the SC system. It is noteworthy that the DSs system is characterized by a resistance $F_{DS,S} = 588$ kN, and a stiffness $K_{DS,S} = 33.92$ kN/mm. Anchorage plates for the PT bars are welded to the column. Oversized web holes and flange slots are designed to accommodate the target rotation required by the EC 8[3] (i.e., 0.035 rads), plus a tolerance of 0.01 rads. Given the adopted design criteria, the gap-opening of the SC-CB is allowed only when the seismic intensity is higher than the ULS. The design method aims at avoiding the possible failure modes (e.g., yielding of the PT bars and/or bolts reaching the end of their travel paths) up to the target rotation. Table 3 lists the geometrical configuration and the design input actions of the SC-CBs, defined by considering the proper location of the splice. Table 4 summarizes the main geometrical and structural properties of the SC-CB. The FDs' properties are consistent with the FDs of the DF-BCJs.

2.2 | Characterization tests

Coupon tests have been carried out to determine the stress-strain curve of the adopted structural steel and characterize the modulus of elasticity (E), yield stress (σ_y), ultimate stress (σ_u), and the corresponding deformations. S355 steel class was used for beams and columns of the structure, and three coupon specimens (i.e., one web and two flanges) for each element were subjected to tensile tests according to EN ISO 6892-1.[66] The results are listed in Table 5.

Characterization tests have been performed for the FDs to define the interface material's friction coefficient (μ). The tests have been performed on three subassemblages of S355 steel plates and friction pads with thermally sprayed material using the universal machine SCHENCK HYDROPULS S56. The layout was defined similarly to EN1090-2,[67] while the loading protocol was consistent with EN 15129.[68] All tests provided consistent results showing regular hysteretic behavior with a slight kinematic hardening. The dynamic friction coefficient's average value (i.e., $\mu = 0.53$) is consistent with previous tests,[17,18] with a loss of the initial bolts' preload of 15% due to the wearing of the friction interface. It is highlighted that the FD used within this connection has been extensively investigated by previous experimental works through uniaxial tests as well as within the DF-BCJ[19–22] and SC-CB[50] and hence, also including a combination of moments, shear, and axial forces. Moreover, to gain confidence in the FD response, characterization tests have been carried out to evaluate the relationship between the torque (T_b) and bolt preload force (N_b) (i.e., the nut factor k), considering three

TABLE 5 Steel properties: Average values from three coupon specimens.

Profile [–]	σ_y [MPa]	ε_y [%]	E [MPa]	σ_u [MPa]	ε_u [%]
Beam (IPE 270)	412	0.194	211708	532	38.0
Column (HE 200B)	356	0.168	212102	465	32.4

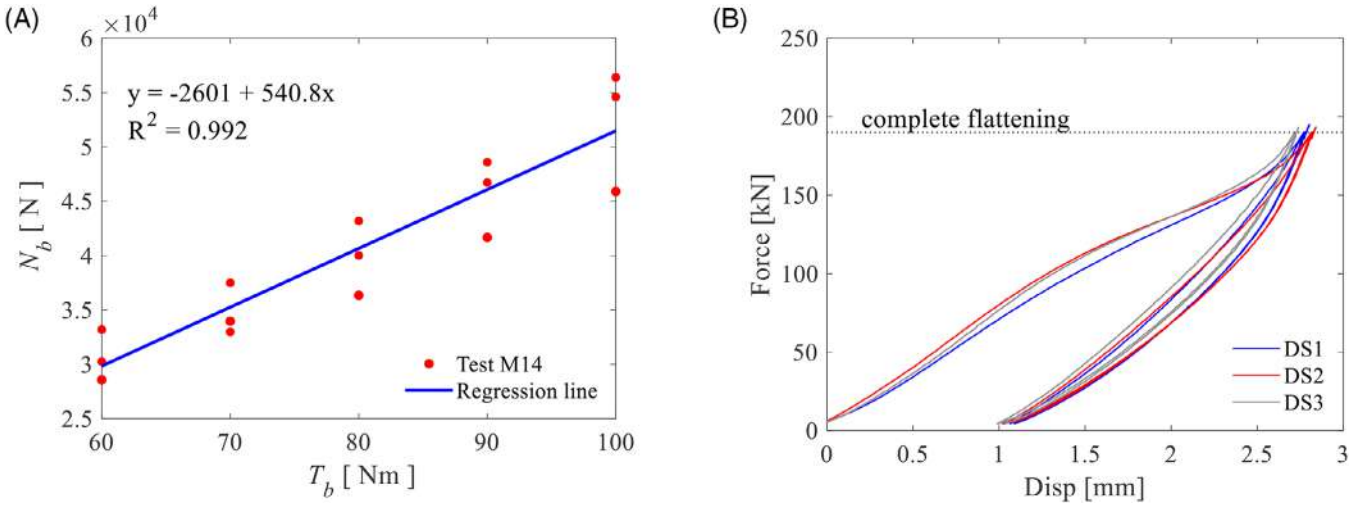

FIGURE 4 Characterization tests: (A) Relationship between T_b and N_b for M14 bolts; (B) DSs pre-setting process.

bolts of each type with different torque values (i.e., T_b from 60 to 100 Nm for M14 and from 120 to 160 Nm for M16). It is noteworthy that these values have been selected within a reasonable range of variation, considering the design torque of the bolts used in the experimental campaign. Regressions of 15 samples for each bolt type provided a k value equal to 0.129, consistent with the manufacturer's recommendations. The results are shown in Figure 4(A) for the M14 10.9 bolts.

The DSs are special washers DIN 6796 installed after a presetting procedure according to DIN 267-26,[70] performed to ensure their elastic response during the tests.[71] The DSs were compressed according to their flattening load (i.e., 196 kN), namely, the force needed to flatten the washer completely. Figure 4(B) shows the force-displacement curves of three DSs specimens (i.e., DS1, DS2, and DS3), highlighting the effect of the presetting procedure (i.e., nonlinear response) and the elastic response during the reloading and unloading phases. It is observed that the DSs show a nonlinear elastic response for higher forces close to their complete flattening. This is further discussed in Section 4.2.

2.3 | Test setup and instrumentation

The experimental setup consisted of two actuators (MTS 243.60-02 and MTS 243.45-01) connected to the structure's first and second floors to apply horizontal loads. The actuators' load capacity in compression and tension, as well as the piston stroke, are illustrated in Figure 1. The two actuators were connected to the deck of the test specimen on one side and fastened to a reaction steel braced frame on the other side. The specimen is connected to the strong floor with rigid and oversized steel footings. Figure 5 shows the instrumentation and measurement devices used for the tests. Wire transducers (WSs) and linear variable differential transducers (LVDTs) were used at each level to measure horizontal displacements and check possible deck rotations. Additionally, the local response of the structure and its components was assessed using axial strain gauges and LVDTs. Four uniaxial strain gauges were installed at the flanges of all columns at top and bottom sections (e.g., 1A-B and 1A-T—see Figure 5) to monitor axial forces and bending moments. In this way, the bending moments at the connection level can be defined using nodal equilibrium. The rotations of the DF-BCJs and SC-CBs were assessed by LVDTs. Finally, load cells and strain gauges were used to monitor tensile forces in the PT bars.

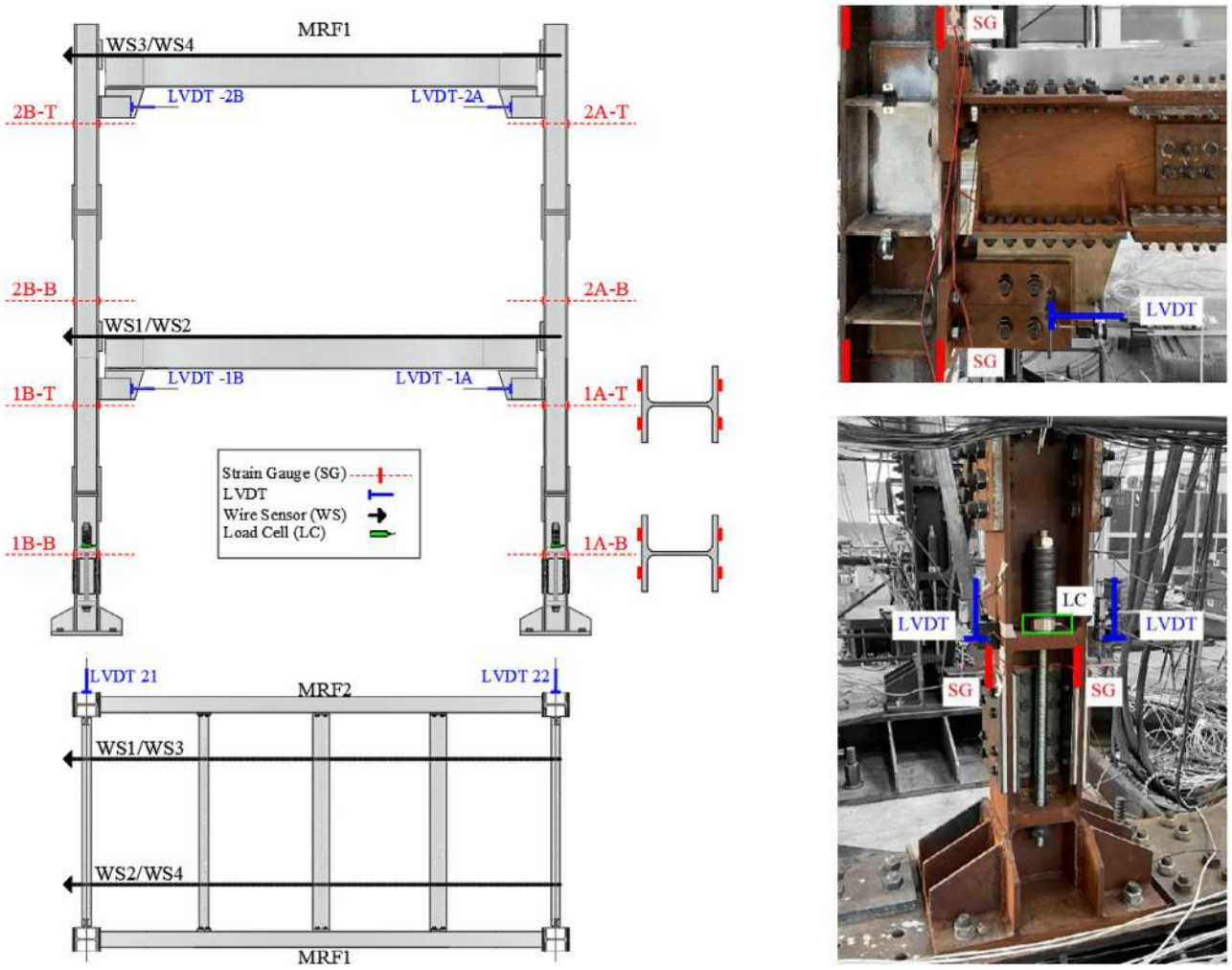

FIGURE 5 Global and local instrumentation.

2.4 | Test matrix

Table 6 reports the matrix for the PsD tests[58] and provides detailed information about the adopted ground motion records. The Pseudo 2 software[72] was used to perform and control the tests, adopting a time step of the motion equations' integration algorithm equal to 0.01 sec. Preliminary tests were carried out to obtain the modal properties of the structure.

TABLE 6 Test matrix.

Test [–]	Input [–]	Station [–]	Date [–]	Direction [–]	Natural PGA [g]	Amplified PGA [g]	$S_{a,PsD}$ (T_1) [g]	$S_{a,PsD}(T_1)/S_{a,ULS}(T_1)$ [–]
1	Imperial Valley	Agrarias, USA	15/10/1979	N/S	0.37	1.10	2.01	1.91
2	Spitak	Gukasian, Armenia	07/12/1988	N/S	0.20	0.80	1.38	1.31
3	Artificial	SIMQKE	–	–	0.35	0.50	1.56	1.48
4	Santa Barbara	Courthouse, USA	13/08/1978	N-S	0.10	0.80	1.16	1.10
5	Coalinga	Slack Canyon, USA	02/05/1983	N/E-S/W	0.17	0.80	1.62	1.54
6	Kobe	Kakogawa, Japan	16/01/1995	N/S	0.26	0.80	1.40	1.33
7[1]	Imperial Valley	Agrarias, USA	15/10/1979	N/S	0.37	1.10	2.01	1.91
8[2]	Imperial Valley	Agrarias, USA	15/10/1979	N/S	0.37	1.10	2.01	1.91

Note: (1) Additional distributed loads; (2) Additional distributed loads and without the PT bars.

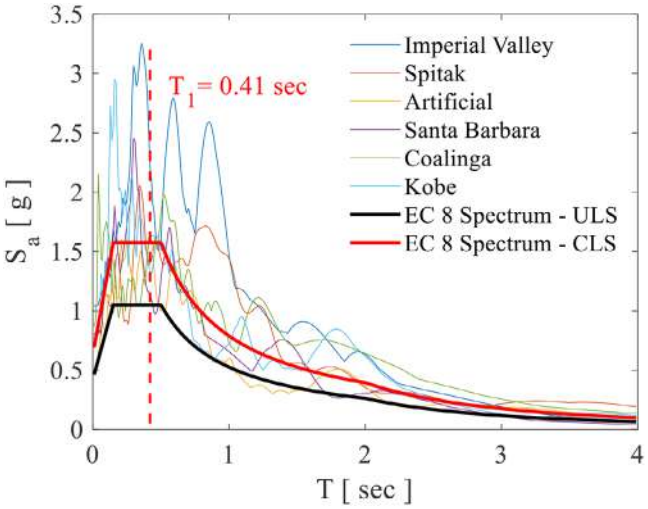

FIGURE 6 Spectra of the amplified records and elastic design spectrum at ULS and CLS.

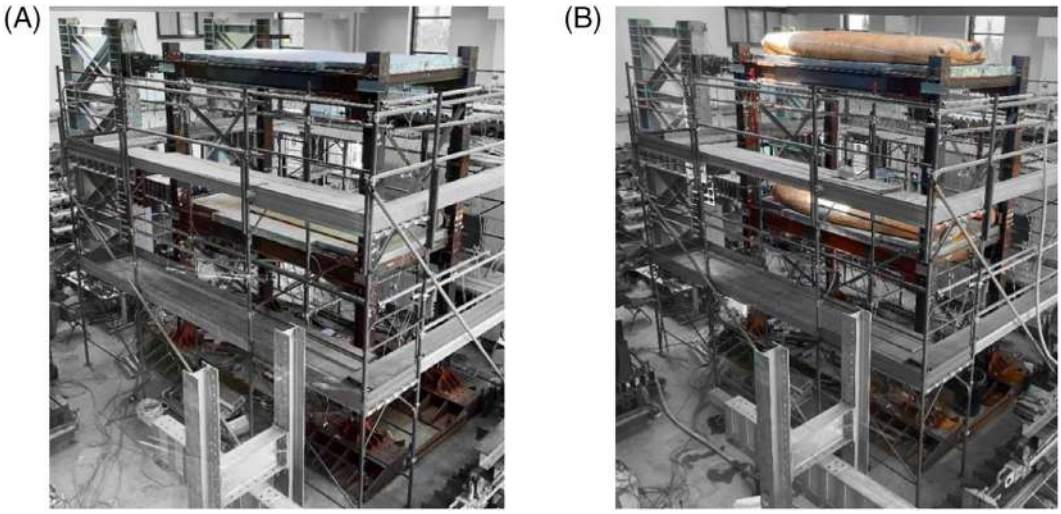

FIGURE 7 Test specimens for: (A) Tests 1–6; (B) Tests 7 and 8.

Subsequently, PsD tests were performed considering five natural ground motion records compatible with the EC 8[3] design spectrum. The mean spectrum of the set of records was kept between 90% and 130% of the corresponding EC 8[3] design spectrum. Additionally, an artificial record was generated by SIMQKE,[73] matching the adopted design spectrum, to investigate the effects of an earthquake characterized by a high energy and frequency content. The ground motion records were amplified to reach intensities compatible with the CLS to investigate the structure's response under large inelastic deformations (Table 6). Figure 6 shows the spectra of the selected accelerograms with amplified PGAs and the elastic design spectrum at ULS and CLS. It is also highlighted that several zero acceleration points were added at the end of each record to allow the free vibrations to stop and capture the residual deformations correctly. Table 6 also lists the spectral accelerations at the fundamental period of the structure ($S_{a,PsD}(T_1)$) for the ground motion records used in the PsD tests (i.e., with amplified PGAs). In addition, also the ratios between $S_{a,PsD}(T_1)$ and $S_{a,ULS}(T_1)$ (i.e., the spectral acceleration of the structure for the ULS, equal to 1.05 g) are reported. Figure 7(A) shows the test specimen for Tests 1–6.

Test 7 was successively carried out to investigate the influence of gravity loads on the SC behavior of the structure. Additional distributed gravity loads at both levels (i.e., 3.50 kN/m^2) were applied with flexible water tanks, as illustrated in Figure 7(B). The following Test 8 was also performed with the additional loads. However, in this case, the PT bars were

removed, and the tightening force of FDs' bolts within the SC-CBs was adequately adjusted to reach the same bending moment corresponding to the gap opening (i.e., M_1).

The structure was repaired at the end of each test. The repair process consisted of two steps: (i) the bolts of the FDs of DF-BCJs and SC-CBs were loosened for residual drift recovery; and (ii) all FDs' bolts and PT bars were retightened to the design preloading force. It is worth mentioning that, in all tests, the initial PT force was always equal to 400 kN for each bar, except for Tests 5 and 6, where it was approximately 350 kN, due to difficulties in the tightening process during testing. However, as discussed in Section 4.2, this aspect did not significantly affect the experimental outcomes. This part of the experimental campaign focused on the evaluation of system-level reparability. On one side, it allowed assessing the complexity of the repair operations; on the other side, it allowed evaluating the effectiveness of the repair strategy in restoring the initial (i.e., undamaged) seismic performance of the structure. It is worth mentioning that, during the whole experimental campaign, none of the elements of the DF-BCJs and SC-CBs were replaced, including the friction pads, bolts, PT bars, and DSs.

3 | RESULTS AND DISCUSSION

3.1 | Modal properties

The stiffness and the modal properties of the specimen were experimentally assessed through white-noise tests. The initial stiffness matrix was experimentally evaluated through preliminary elastic tests. The mass matrix used in the PsD testing procedure was defined considering story masses equal to 38 and 28.4 tons for the first and second stories, respectively. The measured first and second natural periods of the MRFs in the test direction were equal to 0.41 and 0.19 s, respectively. The participating mass of the first mode was equal to 88%. The viscous damping matrix was defined according to the Rayleigh approach, assuming a damping ratio for the two natural modes equal to 3% through the following damping constants: $\alpha_M = 0.3607\ \text{sec}^{-1}$ and $\beta_K = 0.000932$ sec.

3.2 | Global response

After the preliminary tests, the PsD tests were performed according to the Test Matrix (Table 6). Figure 8 illustrates the global EDPs in terms of Interstory Drifts (*IDRs*) and base shear (V_b) time histories for all ground motion records (i.e., Tests 1–6). The maximum values of these quantities (IDR_{Peak} and $V_{b,Max}$) are highlighted for both stories. The residual *IDRs* (IDR_{Res}) are compared with the repairability limits set by FEMA P58-1,[25] corresponding to 0.5% and 0.2%. The results show that the IDR_{Peak} and $V_{b,Max}$ occur at the same instants due to the regularity of the structure and predominance of the first vibration mode.

Figure 8(A) shows the global results for Test 1 (i.e., Imperial Valley—PGA = 1.10 g). This accelerogram was characterized by several peaks of significant amplitude with the highest PGA among all Tests. The first and second maximum story displacements were equal to 79.38 and 153.70 mm, corresponding to IDR_{Peak} of 3.31% and 3.10%, respectively. The residual displacements were equal to 7.28 and 19.59 mm at the first and second stories, corresponding to IDR_{Res} of 0.30% and 0.51%, respectively. It is highlighted that the first-story $IDR_{Res,1}$ was lower than the permissible residual drift of 0.5%,[24] while the second-story $IDR_{Res,2}$ was practically equal to the limit.

Figure 8(B) shows the global results for Test 2 (i.e., Spitak—PGA = 0.80 g). It is worth highlighting that the time history of this accelerogram was characterized by a single peak leading to a single excursion of the structure beyond the elastic range. The residual displacements were equal to 1.52 and 5.73 mm at the first and second levels, corresponding to IDR_{Res} of 0.06% and 0.18%, respectively. In this case, the structure experienced IDR_{Res} lower than the 0.2% limit[25] at both stories. For Test 3 (i.e., Artificial—PGA = 0.50 g) and 4 (i.e., Santa Barbara—PGA = 0.80 g), the structure remained almost elastic without significant residual displacements (Figure 8C, D). Conversely, for Test 5 (i.e., Coalinga—PGA = 0.80 g) and 6 (i.e., Kobe—PGA = 0.80 g) in Figure 8(E, F), the structure experienced large inelastic deformations. In particular, for Test 5, the structure experienced the highest IDR_{Peak} among all tests. For Test 6, the IDR_{Res} were equal to 0.34% and 0.55% for the first and second stories, respectively. The main results are summarized in Table 7. Additional considerations about Tests 7 and 8 and the structure's repairability and resilience are further discussed in Section 5.

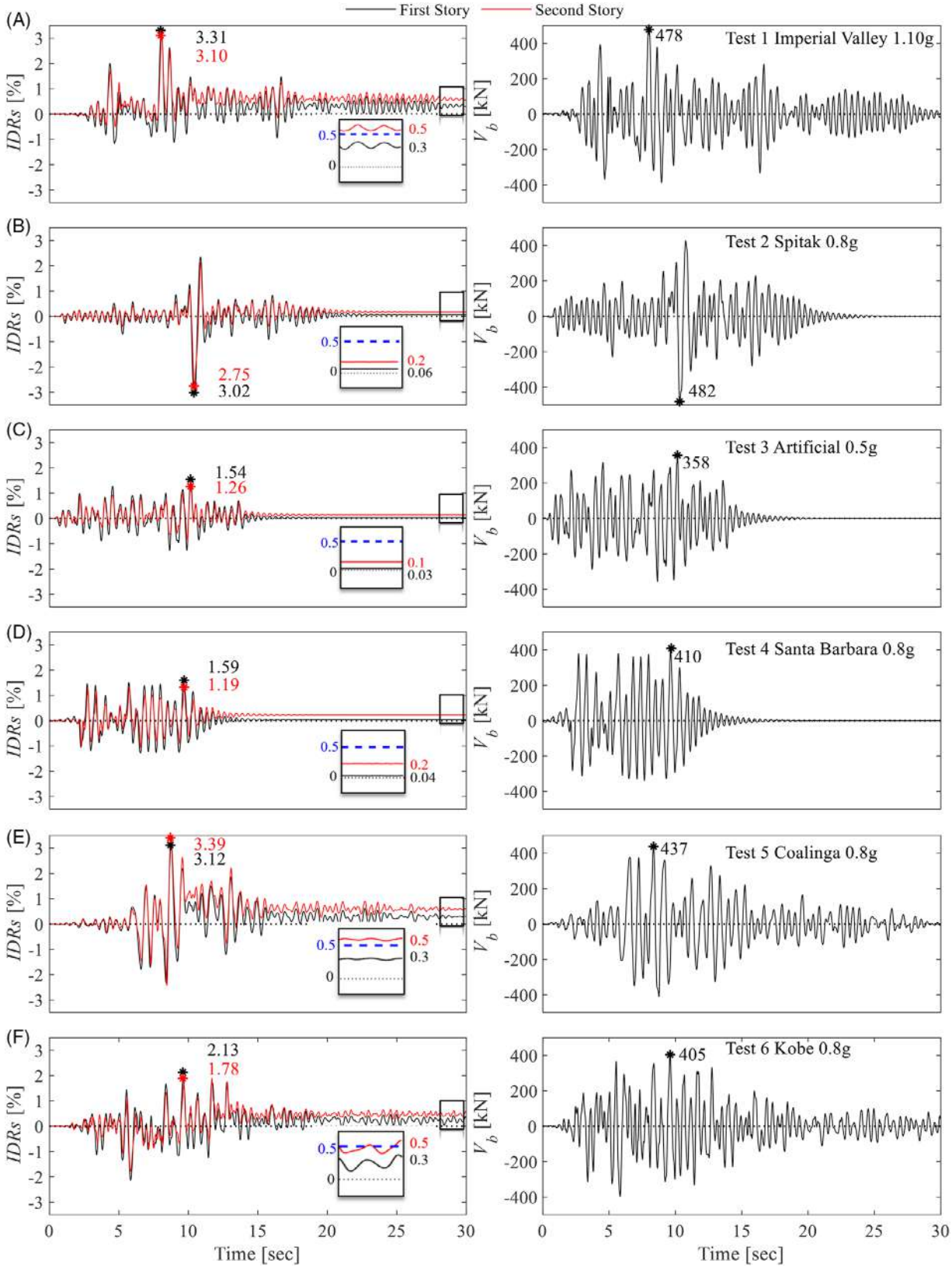

FIGURE 8 Global results in terms of interstory drifts (*IDRs*) and base shear time histories for all tests.

TABLE 7 Global results for all tests.

Test [–]	Input [–]	$d_{Max,1}$ [mm]	$d_{Max,2}$ [mm]	$d_{Res,1}$ [mm]	$d_{Res,1}$ [mm]	$IDR_{Peak,1}$ [%]	$IDR_{Peak,2}$ [%]	$IDR_{Res,1}$ [%]	$IDR_{Res,2}$ [%]	$F_{Max,1}$ [kN]	$F_{Max,2}$ [kN]	$V_{b,Max}$ [kN]
1	Imperial Valley	79.38	153.70	7.28	19.59	3.31	3.10	0.30	0.51	287	286	478
2	Spitak	72.47	138.59	1.52	5.73	3.02	2.75	0.06	0.18	285	288	482
3	Artificial	37.06	67.36	0.65	4.09	1.54	1.26	0.03	0.14	205	209	358
4	Santa Barbara	38.27	66.84	0.88	6.35	1.59	1.19	0.04	0.23	261	237	410
5	Coalinga	74.94	156.22	7.33	20.51	3.12	3.39	0.31	0.54	314	267	437
6	Kobe	51.17	93.86	8.11	21.10	2.13	1.78	0.34	0.55	258	276	405
7[1]	Imperial Valley	78.19	156.60	10.61	26.33	3.25	3.27	0.44	0.65	296	291	472
8[2]	Imperial Valley	86.75	172.74	35.30	74.21	3.58	3.61	1.47[3]	1.62[3]	291	281	449

Note: (1) Additional distributed loads; (2) Additional distributed loads and without the PT bars; (3) Expected to reach large residual drifts.

3.3 | Local responses

Figure 9 shows the local EDPs in terms of moment-rotation of the DF-BCJs (M_{BCJ}-θ_{BCJ}) and SC-CBs (M-$\theta_{SC\text{-}CB}$) for all ground motion records. The hysteretic curves of the DF-BCJs are reported only for two connections (i.e., DF-BCJ 1A for the first story and DF-BCJ 2A for the second story belonging to the MRF-1 – see Figure 1). However, consistent results were observed for the other DF-BCJs and are not reported herein for brevity. The theoretical values of the maximum and minimum bending moments corresponding to the activation of the FDs of the DF-BCJs (M_{slip} = 118 kNm) are reported in black dotted lines. In addition, the values of the moment corresponding to the maximum rotation (M_2) in the SC-CBs are reported in the figure. Generally, it is possible to observe that the DF-BCJs experienced wide and stable hysteretic moment-rotation curves, as expected. The SC-CBs are characterized by hysteretic flag-shaped moment-rotation responses consistent with the theoretical model. In addition, the columns remained elastic, as highlighted by the strain gauge readings in Section 3.4. It is worth mentioning that additional local results are provided in the following section, together with the validation of the numerical model in Section 4.

Figure 9(A) shows the local results for Test 1 (i.e., Imperial Valley—PGA = 1.10 g). The moments of the DF-BCJs at the first story reached values of the maximum and minimum bending moments of 135 and 122 kNm (in absolute values) consistent with the design values (M_{slip}). The small differences can be attributed to the uncertainties related to the friction coefficient and bolt preloading forces. The DF-BCJs at the first story experienced peak rotations of about 0.02 rads (see Figure 9A), while those at the second story were slightly lower. The SC-CBs show the expected flag-shaped hysteretic behavior with negligible residual rotations (i.e., 0.001 rads). In addition, it is observed that the SC-CB experienced only positive values of rotations up to 0.02 rads due to the properties of the seismic record, which is characterized by peaks of high amplitude only in the positive direction. The moment corresponding to the gap opening (M_1) was consistent with the design value. The maximum moment in the experimental test was lower than the maximum moment (M_2) as the peak rotation reached by the joint (i.e., 0.02 rads) was lower than the target rotation.

Figure 9(B) shows the local results for Test 2 (i.e., Spitak—PGA = 0.80 g). Similarly to Test 1, the hysteretic curves of the DF-BCJs at the first and second stories experienced similar responses, consistent with the theoretical values. The SC-CB exhibited a flag-shaped hysteretic response with a higher dissipative behavior than the previous case, with rocking in both directions. It is worth mentioning that, considering that the Spitak accelerogram was characterized by one main large amplitude cycle, it was expected and experimentally confirmed that the FDs of DF-BCJs and SC-CBs exhibited only one nonlinear excursion for both directions.

Differently from Tests 1 and 2, the DF-BCJs experienced no activation of the FDs and negligible rotations during Tests 3 (i.e., Artificial—PGA = 0.50 g) and 4 (i.e., Santa Barbara, PGA = 0.80 g). A similar response was also observed in the SC-CBs, which experienced moderate sliding characterized by a maximum rotation of 0.005 rad in both tests (Figure 9(C) and (d)). Conversely, for Test 5 (i.e., Coalinga—PGA = 0.80 g) in Figure 9(E), the DF-BCJs provided the highest energy dissipation with several hysteretic loops with rotations up to 0.02 rads in both directions. A similar behavior was also observed in the SC-CBs. Similar results, but with lower rotations, were observed during Test 6 (i.e., Kobe—PGA = 0.80 g), as shown in Figure 9(F). The main results are summarized in Table 8. It is highlighted that, as expected, the peak rotations did not exceed the permissible design value (i.e., 0.035 rad) for both DF-BCJs and SC-CBs. Additional considerations about Tests 7 and 8 and the joints' repairability are reported in Section 5.

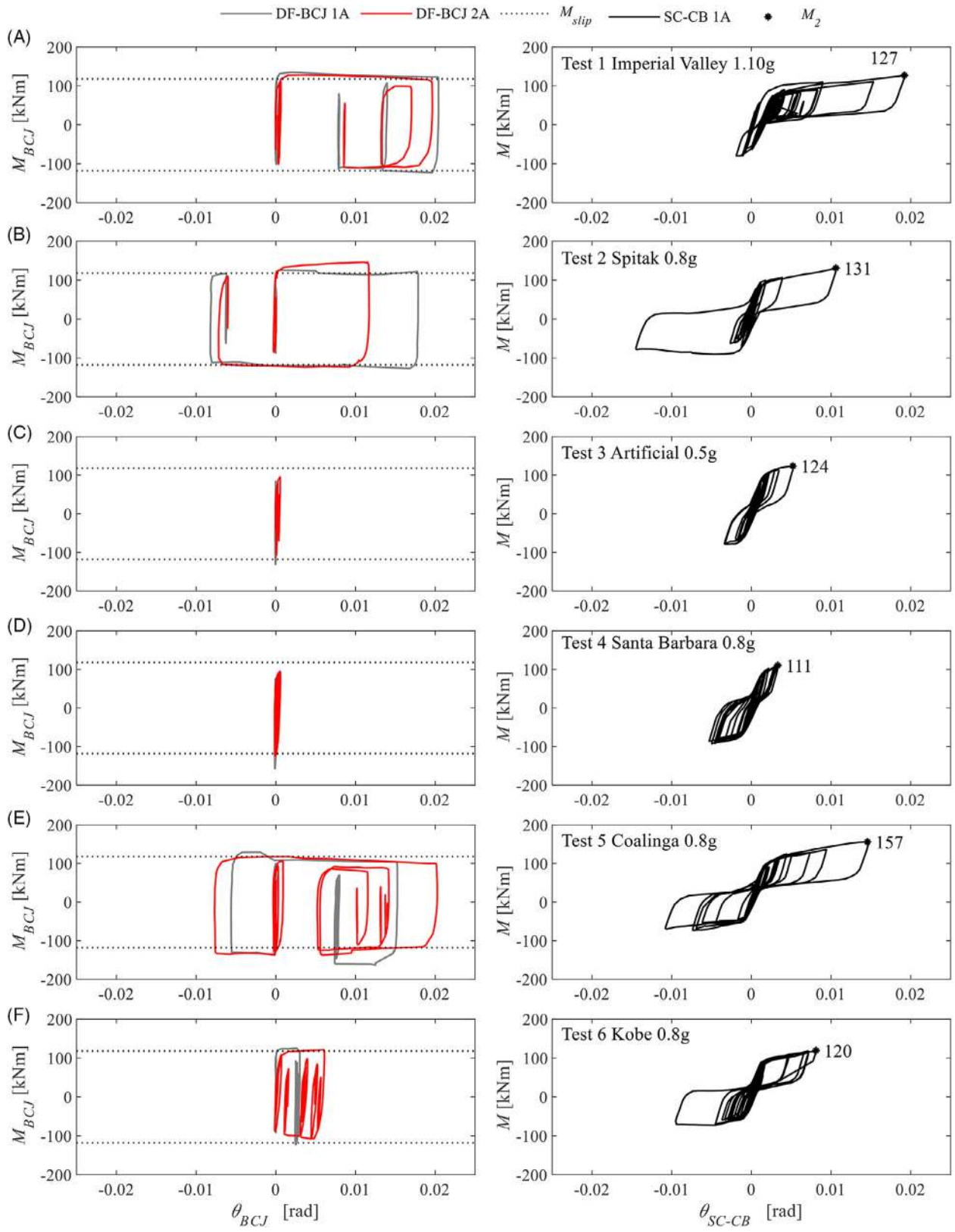

FIGURE 9 Local results in terms of moment-rotation curves for all tests.

TABLE 8 Local results for all tests.

Test [−]	Input [−]	$M_{BCJ,\ Max,1}$ [kNm]	$M_{BCJ,\ Max,2}$ [kNm]	$\theta_{BCJ,\ Max,1}$ [mrad]	$\theta_{BCJ,\ Max,2}$ [mrad]	M_1 [kNm]	M_2 [kNm]	$\theta_{SC\text{-}CB,\ Max}$ [mrad]
1	Imperial Valley	135, −122	128, −110	20.4	19.6	98.1	128	19.2, −1.9
2	Spitak	127, −126	124, −126	17.9	11.7	95.5	131	10.6, −14.5
3	Artificial	84, −131	96, −107	≅0	≅0	96.1	124	5.2, −3.3
4	Santa Barbara	75, −128	95, −124	≅0	≅0	90.1	111	5.3, −3.3
5	Coalinga	129, −133	118, −137	20.5	15.2	99.5	157	14.5, −10.8
6	Kobe	123, −125	108, −122	3.0	6.5	88.4	120	8.1, −9.3
7[1]	Imperial Valley	116, −117	111, −107	22.7	23.9	95.9	133	16.0, −5.0
8[2]	Imperial Valley	121, −104	129, −98	17.4	26.1	67	130	20.0, −2.1

Note: (1) Additional distributed loads; (2) Additional distributed loads and without the PT bars.

3.4 | Test observations

Figure 10(A) shows the SC-CB displaced configurations at the onset of rocking on the right edge for rotations of 0.02 rads. Figure 10(B) shows the strains (ε_c) time histories of the bottom (1A-B and 1B-B) and top sections (1A-T and 1B-T) of the first story columns, obtained from the strain gauges applied to the columns' flanges. For the sake of brevity, results are shown only for the first-story columns of the MRF-1 and for Test 1. However, consistent results are observed for the first-story columns of the MRF-2 and for all the tests. As observed, the first-story columns experienced no yielding, as the strains were lower than the yielding strain ($\varepsilon_{c,y}$) obtained from the coupon tests of Section 2.2. In addition, it is worth mentioning that slight residual deformations are observed at the end of Test 1, due to the residual deformations experienced by the structure. Conversely, the energy dissipation was only provided by the sliding mechanism in the FDs of the DF-BCJs and SC-CBs. In fact, the friction pads of the FDs of both DF-BCJs and SC-CBs experienced wearing, which was clearly observed after the end of the experimental campaign. On the contrary, it is worth mentioning that previous experimental tests on the same structure equipped only with DF-BCJs and subjected to the same test sequence exhibited damage at the first-story columns, which was physically recognized by the yield lines appearing on the surface of the columns.[23]

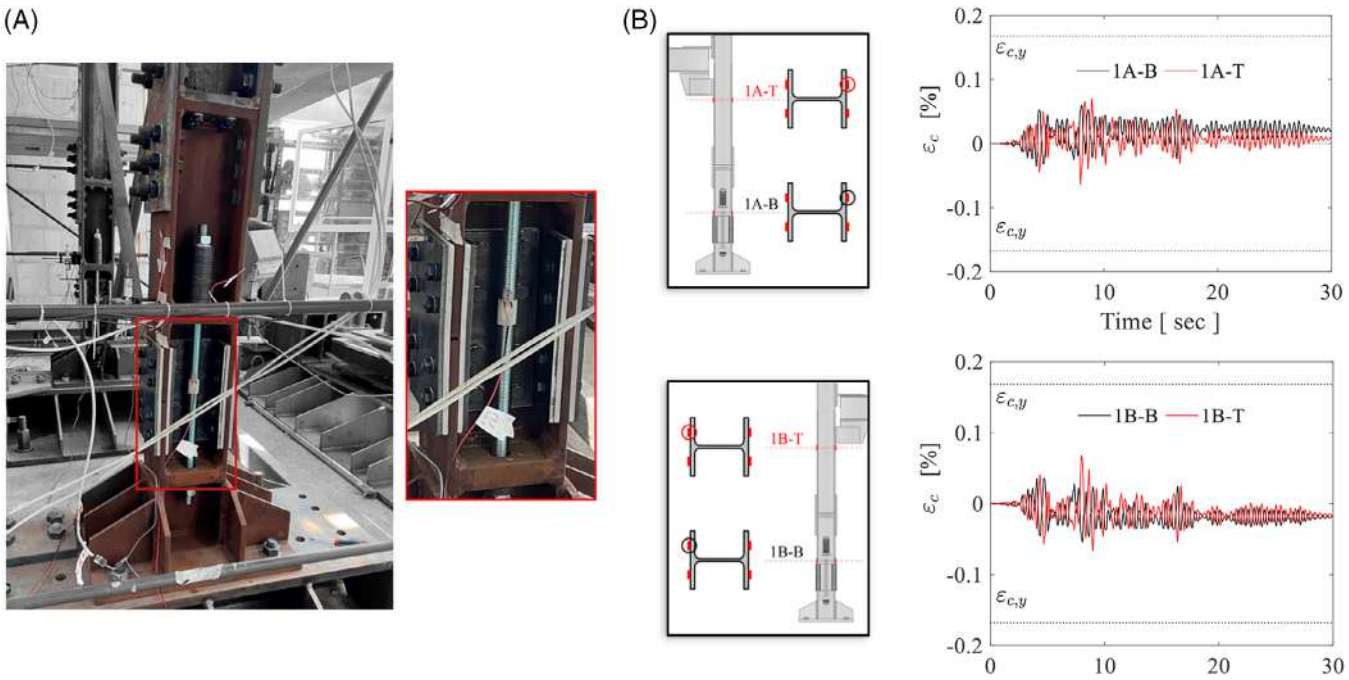

FIGURE 10 Test observations. Self-Centering Column Base (SC-CB): (A) rocking on the right edge with 0.02 rads; and (B) moment-curvature hysteretic behavior of the bottom and top sections of the first story columns.

4 | COMPARISON OF TEST AND NUMERICAL RESULTS

4.1 | Finite element modeling

A 2D nonlinear FE model of one of the MRFs was developed in OpenSees[62] (Figure 11A) to achieve the following objectives: (i) to validate the modeling strategy considering both the local and global EDPs, hence increasing the confidence in the numerical results; (ii) to extend the experimental observations through numerical simulations considering different seismic intensities and different records; and (iii) to generalize the research outcomes through numerical simulations of additional case studies structures in future research works.

The modeling strategy is based on a mixed lumped and distributed plasticity approach. Beams and columns are modeled with inelastic displacement-based *"nonlinearBeamColumn"* elements computed in four integration points. Each fiber section is discretized into eight fibers along with the web and four along each flange. Both beams and columns are defined by the uniaxial "*Steel01*" material with 356 and 412 MPa yield strength, respectively, and a 0.2% postyield stiffness ratio, according to the results of the coupon tests. The stiffness of the section is defined considering both the contributions of axial and shear stiffnesses through the *"section Aggregator*" function. Geometric nonlinearities are considered through the *"PDelta Transformation*." The rigid-floor diaphragm is modeled by assigning a high value to the axial stiffness of the beams. Gravity loads are applied uniformly distributed on the beams. The lumped masses are concentrated at the center of the spans at the level of the actuators' axis, hence simulating the actual location of the forces' application point. Damping sources other than the hysteretic energy dissipation are modeled through the Rayleigh damping matrix, which is compatible with the model used for the PsD testing procedure. The mass-related and stiffness-related damping coefficients are considered for a damping factor equal to 3% for the first two vibration modes.

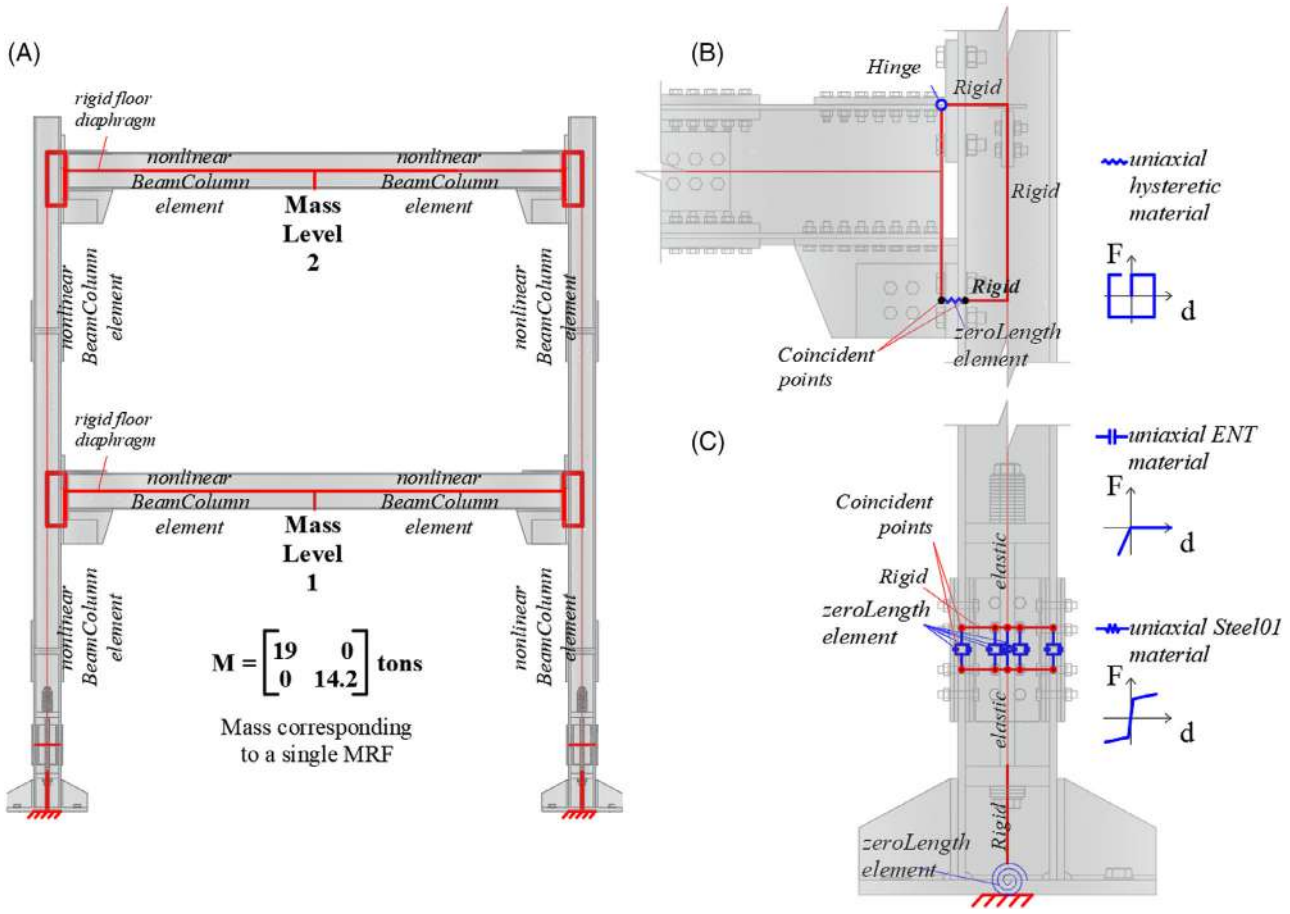

FIGURE 11 2D model in OpenSees.[62]

Figure 11(B) shows the DF-BCJ modeling strategy previously validated against component tests' results by Di Benedetto *et al.*[23] The rigid offsets of the joints are modeled with *"elasticBeamColumn*" elements, assigning them a high flexural stiffness. The COR is located at the T-stub level and modeled as a hinge. The FD is placed at the damper's centreline and modeled by a translational spring represented by a *"zeroLength"* element. This is defined by the uniaxial *"Hysteretic*" material with a symmetric rigid-plastic constitutive law.

Figure 11(C) shows the SC-CB modeling strategy previously validated against component tests' results by Elettore *et al.*[51] It consists of a 2D nonlinear FE model where the rocking interface is modeled with eight rigid *"elasticBeamColumn"* elements with high flexural stiffness (i.e., rigid elements). The web and flanges FDs are modeled with four translational springs represented by *"zeroLength"* elements. They are defined by the uniaxial *"Steel01*" material, with a rigid plastic constitutive law. The rocking behavior is modeled with four translational *"zeroLength*" elements defined by the compression-no-tension uniaxial *"ENT*" material with a high value of the compression stiffness to capture the contact behavior. The SC system is modeled with a single translational spring represented by a single *"zeroLength"* element, which is representative of the SC system composed of PT bars and DSs. It is defined by the uniaxial *"Steel01*" material, with bilinear elastic-plastic behavior, with an elastic stiffness equal to the equivalent stiffness of the SC system and the yield strength of the SC system obtained from the design procedure. The initial PT (i.e., 400 kN) force is modeled by imposing an initial strain using the uniaxial *"InitStrainMaterial*." The stiffness of the DSs system is evaluated based on the tangent stiffness of the isolated DS subjected to the initial PT force (see Figure 4B). An additional rotational spring with uniaxial *"Elastic*" material is included at the base plate level of each first-story column to account for the deformability of the test setup.

4.2 | Validation

The modeling strategy was validated by comparing the FE model in OpenSees[62] against the experimental results for all tests. The validation process was performed for global and local EDPs, including the local behavior of DF-BCJs and SC-CBs. The results for the global EDPs are shown considering the base shear of the whole structure. For validation purposes, quasi-static analyses have been performed by applying the horizontal displacement time histories obtained from the experimental results. The input displacements have been applied to two control points at the first and second stories corresponding to the actuators' application points. The modeling validation results are shown only for Tests 1 and 2. However, consistent results are obtained for all other cases.

Figure 12 shows the displacements and the actuator forces (required to impose the displacements time history) at the first and second stories of the structure for Test 1 (Imperial Valley—PGA = 1.10 g). There is a perfect match of the displacements as these were imposed in the numerical model based on the experimental results. The comparison in terms of forces shows a satisfactory agreement between the numerical and experimental results. The OpenSees results overestimate the first story forces by ~15% and underestimate the second story forces by ~10%. This effect can be attributed to the contribution of the tests' setup flexibility at the column's base connections, which is simulated in the numerical model in a simplified way. The comparison of the base shear shows a more accurate match between the numerical and experimental results (i.e., 5% error).

Figure 13 compares the numerical and the experimental results for one DF-BCJ and SC-CB for Test 1 (i.e., hysteretic behavior, PT force variation). The comparisons are shown for the DF-BCJ 1A and SC-CB 1A; however, consistent results are observed for the other connections. Figure 13(A) shows the numerical and experimental moment-rotation curves of the DF-BCJ. The comparison highlights that the numerical model accurately captures the moments corresponding to the activation of the FDs, with a slight overestimation of the maximum rotation. Figure 13(B) compares the moment-rotation curves of the SC-CB. The comparison evidences that the numerical model captures the local response reasonably well. Nevertheless, some limitations can be highlighted. In particular, the numerical model shows a slightly higher strain-hardening behavior with respect to the experimental results. This effect is mainly due to the loss of preloading forces in FDs' bolts and PT bars experienced during the experimental tests and not simulated in the numerical model (see Figure 13C).[69] The initial PT force was equal to 400 kN for each bar, with minimal variations from bar to bar. Successively, the evolution of the PT force was consistent between the PT bars and reached a reduction of approximately 25%, after which it stabilized. This PT force loss occurred due to small nonlinear mechanisms experienced by the SC system, including minor plastic deformations of the PT bars (i.e., maximum measured PT force equal to 610 kN—nominal yielding strength of the PT bars corresponding to 522 kN) and limited

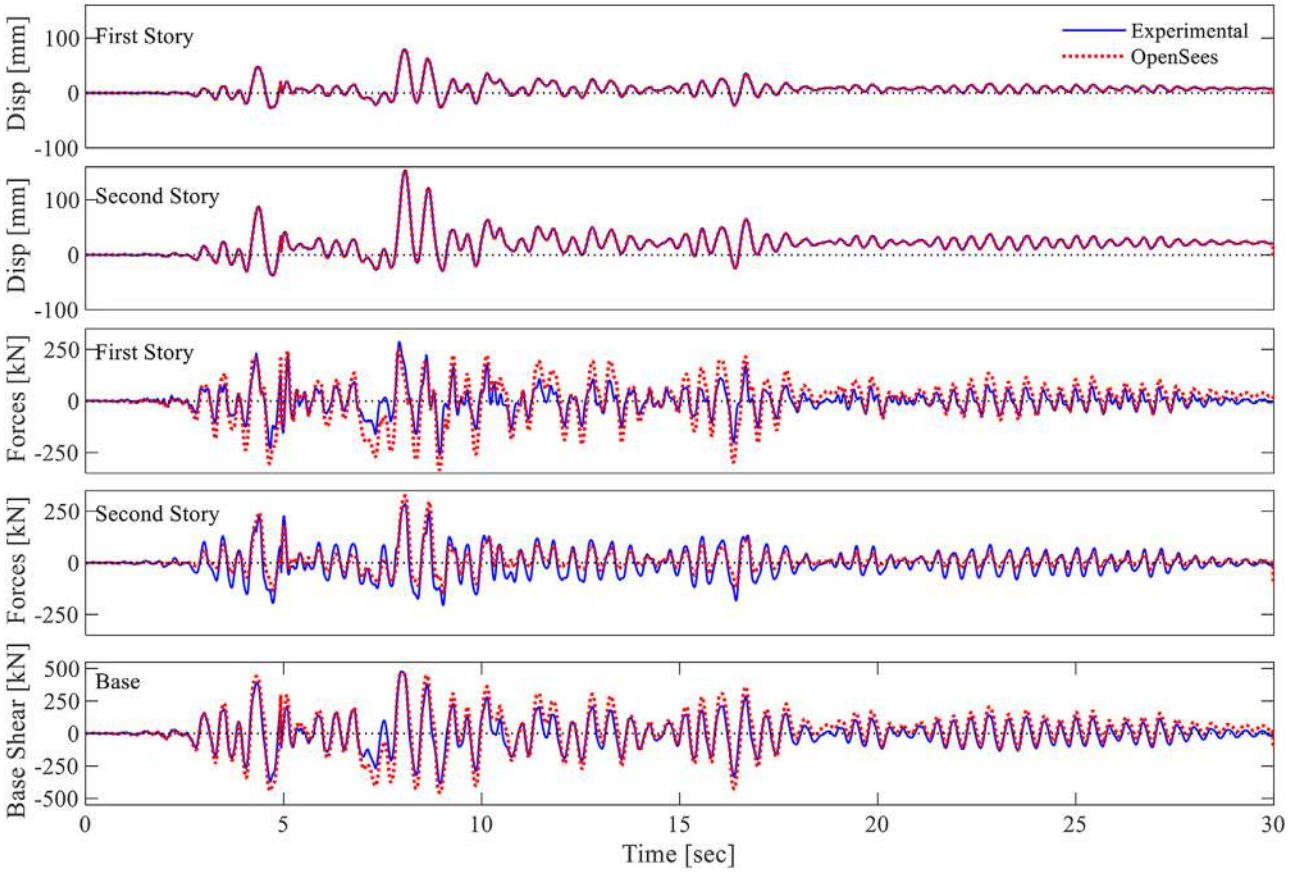

FIGURE 12 FEM validation. Displacements and actuator forces for Test 1 (Imperial valley—PGA = 1.10 g).

nonlinear response of the DSs. The comparison of the results highlights that the numerical model successfully captures the increase in the PT force up to approximately 10 sec (Figure 13C), while some differences can be observed for the following part of the test. Figure 13(D) shows the tension force variation in the PT bars versus the joint rotation.

It is noteworthy that the modeling strategy could be improved by accounting for the PT force loss as previously done in the literature.[69] However, the comparisons carried out by considering the upper and lower bounds of the PT force showed only a minor improvement in the SC-CB response prediction (i.e., numerical simulation with the lower bound reduced the error from 15% to 6% in the peak moment and from 8% to 5% in the peak rotations with respect to the simulations with the upper bound). Although the lower bound shows a slightly better match, the PT force degradation cannot be easily predicted, and hence it is not practical to be used in the numerical models. Hence, the current modeling strategy represents a compromise between accuracy of the results and complexity/computational cost of the model/simulations.

Similarly, Figure 14 compares the numerical and experimental local results for Test 2. Figure 14(A) compares the hysteretic curves of the DF-BCJ, highlighting a satisfactory match of the results, with the numerical model only slightly overestimating the maximum rotations. Figure 14(b) compares the moment-rotation behavior of the SC-CB. It is highlighted that there is no SC behavior for one of the cycles, which may be related to the interaction of bending moments with tensile axial forces in the column. However, this did not affect the SC capability of the connection during the following cycles. Compared to Test 1, this test was characterized by a lower PT force loss during the loading history, illustrated in Figure 14(B). Figure 14(C) shows the tension force variation in the PT bars versus the joint rotation, exhibiting the same stiffness for negative and positive rotations. Results for the other tests are not shown for brevity. However, no significant PT force loss was observed in Tests 3, 4, and 6, and all components remained elastic. Conversely, in Test 5, the PT bars experienced small plastic deformations. However, the consequent slight reduction of PT force did not significantly affect the SC-CBs' response.

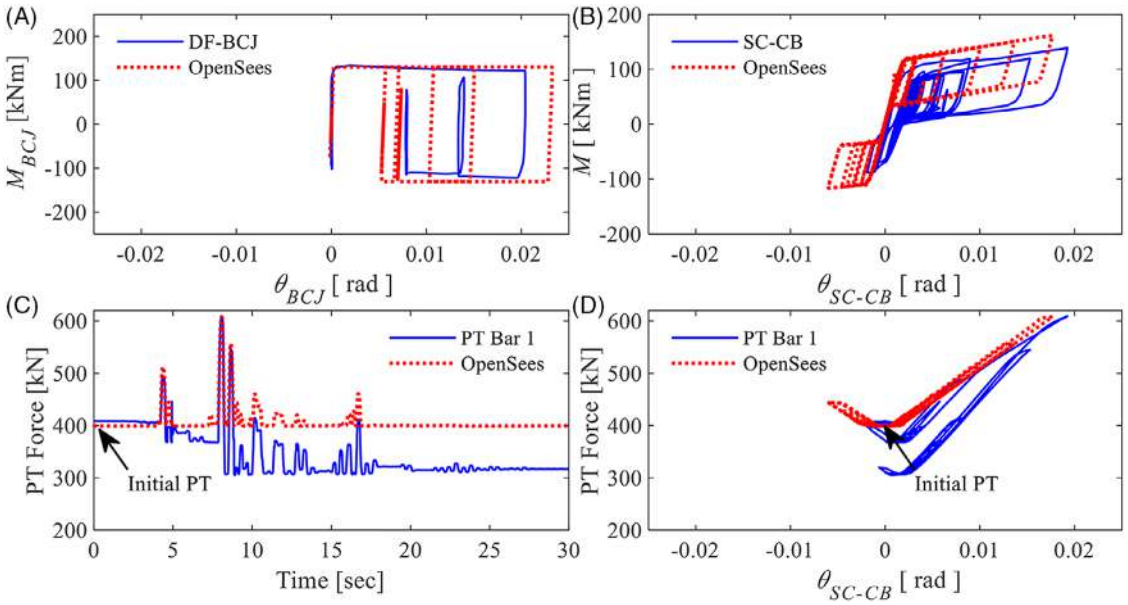

FIGURE 13 FEM validation. Local responses for Test 1 (Imperial Valley—PGA = 1.10 g).

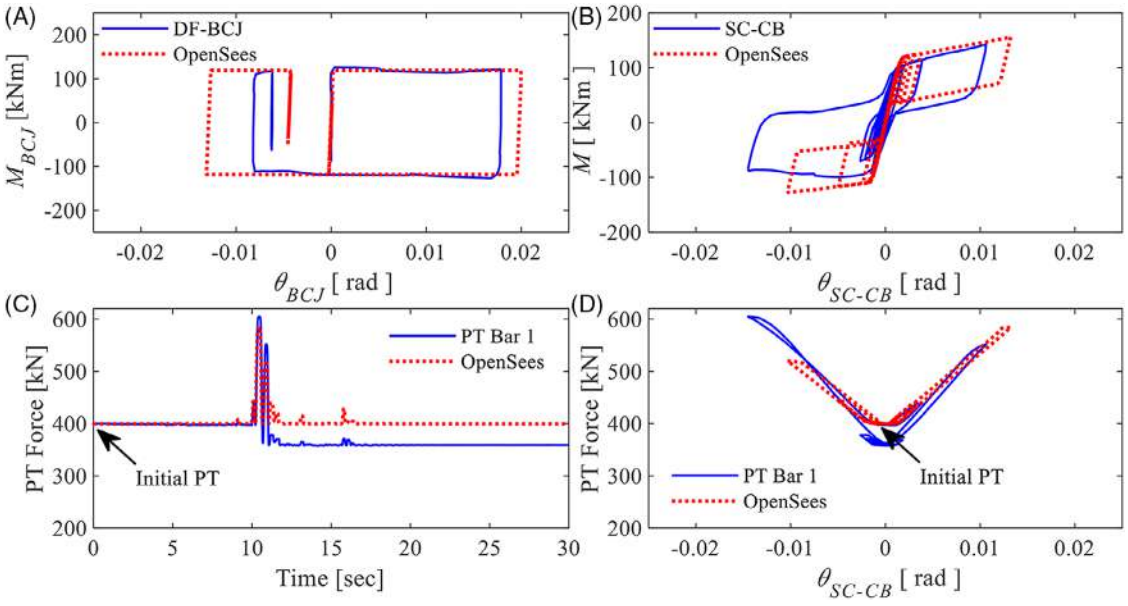

FIGURE 14 FEM validation. Local responses for Test 2 (Spitak—PGA = 0.8 g).

5 | REPAIRABILITY AND RESILIENCE

5.1 | Influence of the PT bars

The Tests Matrix also included Tests 7 and 8, whose results have not been discussed so far. These tests were similar to Test 1 (i.e., Imperial Valley—PGA = 1.10 g) but included additional gravity loads at both levels. Test 8 was performed without the contribution of the PT bars. Figure 15(A, B) compare these three tests in terms of *IDR*s time histories for the first and second stories, respectively. The comparison among the three curves highlights three essential aspects: (i) the negligible influence of the additional gravity loads; (ii) the ability of the repair process to restore the seismic performance of the undamaged structure; and (iii) the crucial role of the PT bars in contributing to the residual drifts' reduction. The comparison between Tests 1 and 7 shows no significant differences in terms of *IDRs*. This was expected due to the limited

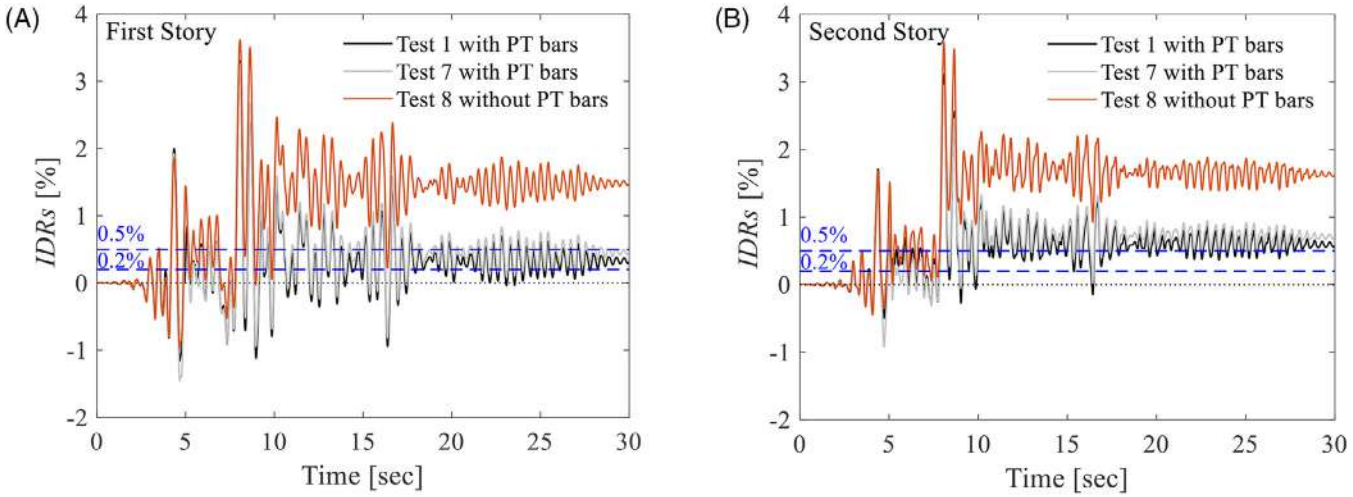

FIGURE 15 Comparison of interstory drifts with and without the PT bars for the: (A) first story; (B) second story.

contribution of the considered additional gravity loads with respect to the applied preload imposed by the PT bars (i.e., 4% of the initial preload for each column). Therefore, in this case, the additional loads did not contribute to the SC behavior, as expected.

Moreover, the match of the responses for Tests 1 and 7 confirms that the relatively 'simple' repair process used in these tests allows for restoring the initial performance of the undamaged structure. On the other hand, the comparison of Tests 1 and 7 with Test 8 shows the crucial role of the PT bars. It can be observed that, in Tests 1 and 7, the introduction of the PT bars allows a significant reduction of the IDR_{Res} for both stories (i.e., from 1.47% to 0.30% for the first story and from 1.62% to 0.51% for the second story), with a slightly decreasing efficiency along the height (i.e., the percentage reduction ranges from 80% to 69% from the first to the second story). These beneficial effects and the limitations of the solution were already highlighted in previous numerical studies by the authors.[51–53]

5.2 | Repairability

As previously mentioned, the structure was repaired at the end of each test. The repair process involved loosening all the high-strength bolts of the FDs of DF-BCJs and SC-CBs (Figure 16) and retightening them to obtain the predefined preloading force. The loosening process consisted of two steps: (i) loosening the bolts belonging to the FDs of the DF-BCJs starting from the second story; (ii) loosening the bolts belonging to the FDs of the SC-CBs. The aim was to investigate the system-level performance recovery in restoring the initial 'undeformed' configuration. The process consisted of loosening 16 bolts of DF-BCJs (i.e., 4 for each joint) and 48 bolts belonging to the SC-CBs (i.e., 12 for each joint). All bolts were loosened with a torque wrench, and the entire operation took approximately 15 min with two people working

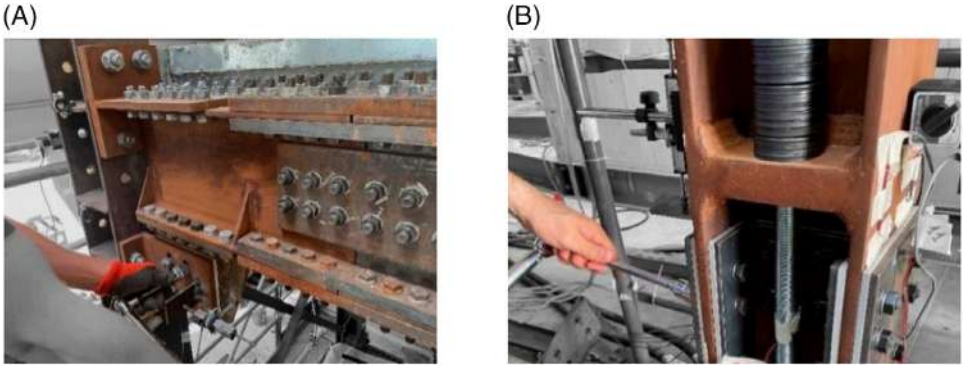

FIGURE 16 FDs bolts' loosening process at the end of each test: (A) DF-BCJs; (B) SC-CBs.

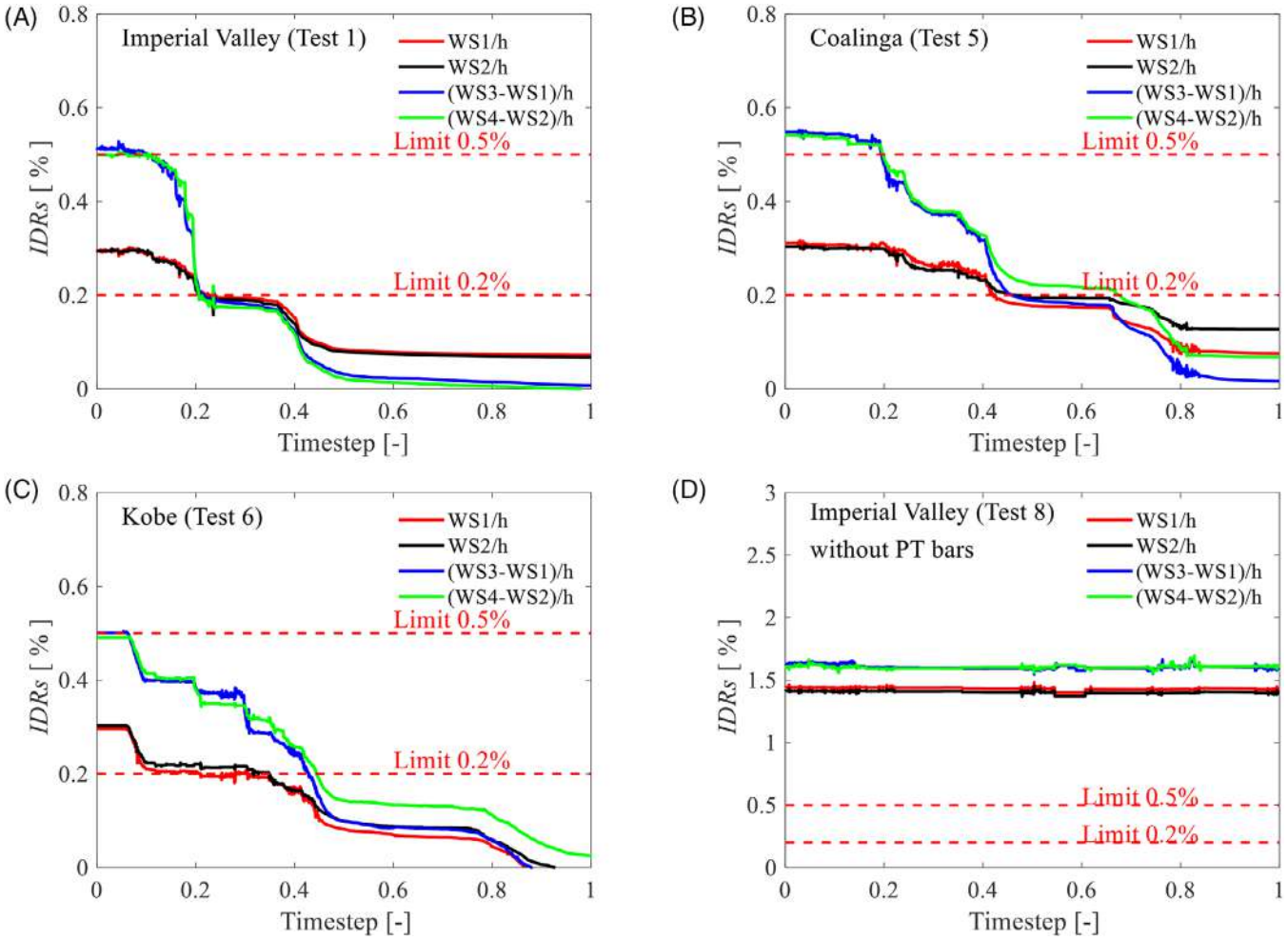

FIGURE 17 Interstory drifts during the bolts' loosening process: (a) Imperial Valley (Test 1); (b) Coalinga (Test 5); (c) Kobe (Test 6); Imperial Valley (Test 8).

simultaneously. The wire sensors were monitored for the first (i.e., WS1, WS2) and the second stories (i.e., WS3, WS4) during the loosening process. It is highlighted that, except for some slight differences, no significant variations were observed from the measurements of the WSs belonging to the same story.

Figure 17(A–C) show the results of the loosening process performed after three tests, that is, Imperial Valley—Test 1, Coalinga—Test 5, and Kobe—Test 6, in terms of *IDRs* vs. Timestep (i.e., time employed to complete the whole repairing process). These tests were selected as they resulted in the highest IDR_{Res} approximately equal to 0.3% at the first story and close to the repairability limit of 0.5%[24] at the second story. The repair process showed that the *IDRs* reduced almost to zero by loosening the FD's bolts of the DF-BCJs and SC-CBs, hence demonstrating the repair method's effectiveness in terms of residual drift recovery. In other words, the structure can be recentered by loosening the high-strength bolts belonging to the FDs.

The successive step of the repair process of retightening bolts and PT bars took approximately 20 min. Additionally, as discussed in the previous section, it was demonstrated that after each test, the structure always recovered the initial performance, behaving as a 'new' structure even after several tests (i.e., comparison between Test 1 and 7). This consideration, together with the observation of easy and fast repair process (i.e., minimized repair time), highlights the advantages in terms of repairability, functional recovery, and seismic resilience. In addition, the results highlighted that the IDR_{Res} of 0.5%, typically considered as the repairability limit[24] for conventional structures, may not be adequate for innovative structures like the one investigated. In fact, the experimental campaign highlighted the ability of the structural solution to drastically reduce the IDR_{Res} by simply applying easy and quick repair strategies. For comparison purposes, Figure 17(D) shows the effects of the loosening process performed after Test 8 for the specimen without PT bars. The results show that the loosening process was ineffective in reducing the residual drifts due to the absence of the PT bars.

5.3 | Generalization of the results

In this section, IDAs[63] are performed in OpenSees[62] to investigate the PT bars' influence on the frame's seismic response while also considering the influence of record-to-record variability. Three configurations are analyzed and compared: the MRF with the SC-CB modeled as presented in Section 4.1, the equivalent MRF with the SC-CB without the PT bars and the MRF with conventional full-strength CBs.[51] Nonlinear time history analyses are performed by considering a suite of 30 ground motion records selected from the SIMBAD Database[74] with moment magnitude ranging from 6 to 7, epicentral distance R ≤ 30 km, and spectrum-compatibility in the range of periods between 0.2 T_1 and 2 T_1. The mean elastic spectrum of the set is kept between 75% and 130% of the corresponding EC 8 based elastic response spectrum.[3] The spectral acceleration corresponding to the first vibration mode (i.e., $S_a(T_1)$) is used as Intensity Measure (IM), where T_1 = 0.41 s for all structures. S_a (T_1) is equal to 0.52, 1.05, and 1.58 g, respectively, for the DLS, ULS, and CLS, representing the seismic intensities of interest. IDR_{Peak} and IDR_{Res} are recorded as global EDPs to analyze and compare the seismic performance of the three structural systems.

Figure 18 illustrates the comparison of IDR_{Peak} and IDR_{Res} versus IM for the structure with, without PT bars and with conventional full-strength CBs. Bold lines represent the mean responses among all ground motions, while thin lines show the single IDA curves. For the sake of brevity, results are shown only for the first story; however, the second story shows consistent trends. The limits threshold of 0.2% for structural realignment,[24] 0.5% for reparability,[25] and 1%[3] for the DLS requirements are also included. Figure 18 (A) shows that the introduction of PT bars does not significantly affect the peak values of the seismic demands in terms of global EDPs. It is also highlighted that the three structures achieve mean values of the IDR_{Peak} lower than the 1% threshold[3] under the DLS, as expected from the design.[3] On the other end, Figure 18 (B) shows the contribution of the PT bars in significantly reducing the IDR_{Res} across the entire range of IM values investigated. In particular, the MRF with PT bars experiences IDR_{Res} lower than the 0.2% threshold[24] in terms of mean response, even for the CLS, at both stories. This effect represents a considerable benefit in terms of structure's repairability. Conversely, this limit is never satisfied for the equivalent structure without PT bars and for the MRF with conventional CBs at both the ULS and CLS. Moreover, the 0.5% threshold[25] is not satisfied in terms of mean response at the CLS, for both the structure without PT bars and for the MRF with conventional CBs.

It is worth mentioning that the IDAs are also performed with and without the leaning column, which accounts for the presence of the gravity frames of the entire building structure described in Section 2.1, following a consistent approach with Elettore *et al.*[51] However, no significant differences are observed for the considered EDPs while considering the contribution of the leaning column.

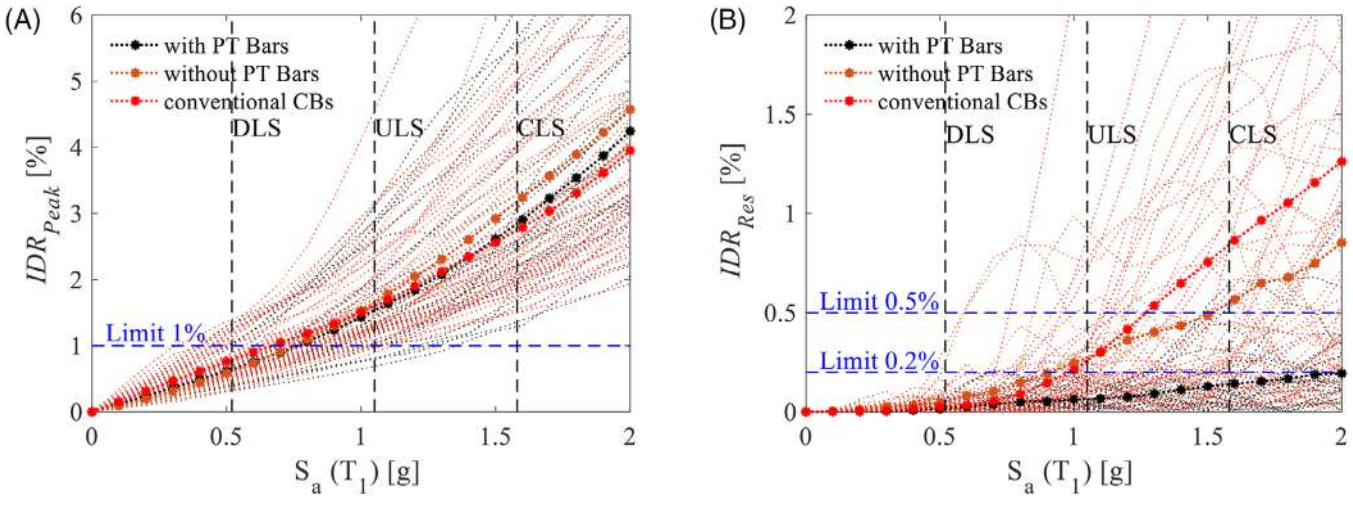

FIGURE 18 IDAs results. Comparison of the seismic performance with, without the PT bars and with conventional CBs for the first story in terms of (A) Peak interstory drifts (IDR_{Peak}) and (B) Residual interstory drifts (IDR_{Res}).

6 | CONCLUSIONS

This paper presents an experimental program on a large-scale two-story steel structure equipped with Damage-Free BCJs (DF-BCJs) endowed with FDs and Self-Centering Column Base (SC-CB) connections. The experimental campaign was performed at the STRENGTH Laboratory of the University of Salerno, Italy, through a Pseudo-Dynamic (PsD) testing procedure. The test specimen is first described, including a presentation of the preliminary characterization test for the material properties and components. Then, the experimental program is shown, including the Test matrix, the experimental setup, and the instrumentations. Preliminary white-noise tests with low-intensity earthquakes are conducted to evaluate the dynamic response of the structures in the elastic range. A sequence of eight high-intensity ground motion records is applied to assess the seismic response. Global and local Engineering Demand Parameters (EDPs) are monitored to investigate the influence of the proposed SC-CBs on the seismic performance of the tested structure. Additionally, at the end of each test, the specimen has been repaired by loosening and retightening all the high-strength bolts belonging to the FDs of both DF-BCJs and SC-CBs. Similar operations were performed on the PT bars. A detailed Finite Element (FE) numerical model is developed in OpenSees, and comparisons between experimental and numerical results are presented for two individual ground motions. Finally, Incremental Dynamic Analyses (IDAs) are performed to numerically investigate the PT bars' influence on the structure's seismic response while also considering the influence of record-to-record variability.

The following conclusions can be drawn: (i) the experimental results demonstrate the effectiveness of the SC-CBs in limiting the residual drifts on the whole structure below the acceptable drift limit for reparability of 0.5%; (ii) the peak rotations do not exceed the permissible design value (i.e., 0.035 rad) for both DF-BCJs and SC-CBs; (iii) the first story columns are fully protected from yielding; (iv) the energy dissipation is only provided by the sliding mechanism in the FDs of the DF-BCJs and SC-CBs; (v) the tests performed with and without the PT bars demonstrate the paramount role of the PT bars in allowing a significant reduction of the residual interstory drifts at both stories (i.e., from 1.47% to 0.30% for the first story and from 1.62% to 0.51% for the second story), with a slightly decreasing efficiency along the height (i.e., the percentage reduction ranges from 80% to 69% from the first to the second story). In addition, the PT bars do not produce any detrimental effect on the peak values of the seismic demands; (vi) the repair process (i.e., loosening all the high-strength preloadable bolts of the FDs of both DF-BCJs and SC-CBs) and the retightening of the PT bars applied after each test is effective in reducing the residual drifts almost to zero and in restoring the seismic performance of the undamaged structure. Conversely, for the equivalent structure without the PT bars, the repairing methodology is ineffective in reducing the residual drifts; (vii) the numerical modeling approach allows the prediction of the global structural response with accuracy. The limitations of the modeling strategy in predicting the local response are also highlighted and discussed; and (viii) the IDA results provide a more exhaustive view into the structure's reparability and resilience for seismic intensities different from those of the tests.

ACKNOWLEDGMENTS

The research activity herein presented was partially supported by the European Community by research grant RFSR-CT-2015-00022. In addition, this research was supported by the UCL Global Engagement Office under the 2020/21 Global Engagement Funded project *'Full-scale pseudo-dynamic experimental Test of a seismic-resilient steel moment resisting frame equipped with damage-free self-centering column bases'*. The Authors also acknowledge the support from the Royal Society—International Exchange program under the grant agreement IES\R3\213175. Any opinions, findings, conclusions and/or recommendations expressed in this paper are those of the authors and do not necessarily reflect the views of the Funders. Lastly, thanks are extended to Dr. Eng. Francesco Perri and Eng. Ciro Esposito for the technical support during the experimental tests.

DATA AVAILABILITY STATEMENT

The data that support the findings of this study are available from the corresponding author upon reasonable request.

ORCID

Elena Elettore https://orcid.org/0000-0002-0477-2855
Fabio Freddi https://orcid.org/0000-0003-2048-1166
Massimo Latour https://orcid.org/0000-0001-9597-9503
Vincenzo Piluso https://orcid.org/0000-0002-4630-5614
Gianvittorio Rizzano https://orcid.org/0000-0002-9408-0712

REFERENCES

1. Mazzolani FM, Piluso V. In: , ed. *Theory and Design of seismic resistant steel frames*. 1st ed. An imprint of Chapman & Hall; 1996.
2. Faella C, Piluso V, Rizzano G. *Structural steel semirigid connections*. CRC Press; 2000.
3. EN 1998-1, *Eurocode 8: Design of structures for earthquake resistance—Part 1: General rules, seismic actions and rules for buildings*, European Committee for Standardization; 2004.
4. ANSI/AISC 341-16, *Seismic provisions for structural steel buildings*. American Institute of Steel Construction; 2016.
5. ASCE/SEI 7–16, *Minimum design loads and associated criteria for buildings and other structures*, American Society of Civil Engineers; 2017.
6. Okazaki T, Lignos DG, Midorikawa M, Ricles JM, Love J. Damage to steel buildings observed after the 2011 Tohoku-oki earthquake. *Earthquake Spectra*. 2013;29(1):219-243. doi:10.1193/1.4000124
7. Freddi F, Novelli V, Gentile R, et al. Observations from the 26th November 2019 Albania earthquake: the earthquake engineering field investigation team (EEFIT) mission. *Bull Earthq Eng*. 2021;19(5):2013-2044. doi:10.1007/s10518-021-01062-8
8. Soong TT, Spencer BF. Supplemental energy dissipation: state-of-the-art and state-of-the-practice. *Eng Struct*. 2002;24:243-259. doi:10.1016/S0141-0296(01)00092-X
9. Seo CY, Karavasilis TL, Ricles JM, Sause R. Seismic performance and probabilistic collapse resistance assessment of steel moment resisting frames with fluid viscous dampers. *Earthquake Engng Struct Dyn*. 2014;134(14):2135-2154. doi:10.1061/(ASCE)0733-9445(2008)134:1(3)
10. Freddi F, Tubaldi E, Zona A, Dall'Asta A. Seismic performance of dual systems coupling moment-resisting frames and buckling-restrained braced frames. *Earthquake Engng Struct Dyn*. 2021;50(2):329-353. doi:10.1002/eqe.3332
11. Freddi F, Galasso C, Cremen G, et al. Innovations in earthquake risk reduction for resilience: recent advances and challenges. *Int J Disast Risk Re*. 2021;60:102267. doi:10.1016/j.ijdrr.2021.102267
12. O'Reilly GJ, Goggins J. Experimental testing of a self-centring concentrically braced steel frame. *Eng Struct*. 2021;238:111521. doi:10.1016/j.engstruct.2020.111521
13. Fang C, Wang W, Qiu C, Hu S, MacRae GA, Eatherton MR. Seismic resilient steel structures: a review of research, practice, challenges and opportunities. *J Constr Steel Res*. 2022;191:107172. doi:10.1016/j.jcsr.2022.107172
14. Grigorian CE, Yang TS, Popov EP. Slotted bolted connection energy dissipators. *Earthq Spectra*. 1993;9(3):491-504. doi:10.1193/1.1585726
15. MacRae GA, Clifton GC, Mackinven H, Mago N, Butterworth JW, Pampanin S. The sliding hinge joint moment connection. *Bull New Zealand Soc Earthq Eng*. 2010;43(3):202-212. doi:10.5459/bnzsee.43.3.202-212
16. Khoo HH, Clifton C, MacRae G, Zhou H, Ramhormozian S. Proposed design models for the asymmetric friction connection. *Earthquake Engng Struct Dyn*. 2015;44(8):1309-1324. doi:10.1002/eqe.2520
17. Cavallaro GF, Francavilla AB, Latour M, Piluso V, Rizzano G. Experimental behavior of innovative thermal spray coating materials for FREEDAM joints. *Compos B Eng*. 2017;115:289-299. doi:10.1016/j.compositesb.2016.09.075
18. Latour M, Piluso V, Rizzano G. Experimental analysis of beam-to-column joints equipped with sprayed aluminium friction dampers. *J Constr Steel Res*. 2018;146:33-48. doi:10.1016/j.jcsr.2018.03.014
19. Latour M, D'Aniello M, Zimbru M, Rizzano G, Piluso V, Landolfo R. Removable friction dampers for low-damage steel beam-to-column joints. *Soil Dyn Earthq Eng*. 2018;115:66-81. doi:10.1016/j.soildyn.2018.08.002
20. Tartaglia R, D'Aniello M, Campiche A, Latour M. Symmetric friction dampers in beam-to-column joints for low-damage steel MRFs. *J Constr Steel Res*. 2021;184:106791. doi:10.1016/j.jcsr.2021.106791
21. Francavilla AB, Latour M, Piluso V, Rizzano G. Design criteria for beam-to-column connections equipped with friction devices. *J Constr Steel Res*. 2020;172:106240. doi:10.1016/j.jcsr.2020.106240
22. D'Antimo M, Latour M, Cavallaro GF, Jaspart J-P, Ramhormozian S, Demonceau J-F. Short- and long-term loss of preloading in slotted bolted connections. *J Constr Steel Res*. 2020;167:105956. doi:10.1016/j.jcsr.2020.105956
23. Di Benedetto S, Francavilla AB, Latour M, Piluso V, Rizzano G. Experimental response of a large-scale two-story steel building equipped with low yielding friction joints. *Soil Dyn Earth Eng*. 2021;152:107022. doi:10.1016/j.soildyn.2021.107022
24. McCormick J, Aburano H, Ikenaga M, Nakashima M, Permissible residual deformation levels for building structures considering both safety and human elements. 14th World Conference of Earth Engineering, 2008, Beijing, China.
25. FEMA P58-1. Seismic performance assessment of buildings. *Volume 1-Methodology*. Applied Technology Council; 2012.
26. Chancellor NB, Eatherton MR, Roke DA, Akbas T. Self-centering seismic lateral force resisting systems: high-performance structures for the city of tomorrow. *Buildings*. 2014;4:520-548. doi:10.3390/buildings4030520
27. Ricles J, Sause R, Garlock M, Zhao C. Post-tensioned seismic-resistant connections for steel frames. *J Struct Eng*. 2001;127(2):113-121. doi:10.1061/(ASCE)0733-9445(2001)127:2(113)
28. Kim H-J, Christopoulos C. Seismic design procedure and seismic response of post-tensioned self-centering steel frames. *Earthquake Engng Struct Dyn*. 2009;38:355-376. https://doi.org710.1002/eqe.859
29. Vasdravellis G, Karavasilis TL, Uy B. Large-scale experimental validation of steel post-tensioned connections with web hourglass pins. *J Struct Eng*. 2013;139(6):1033-1042. doi:10.1061/(ASCE)ST.1943-541X.0000696
30. Pieroni L, Freddi F, Latour M. Effective placement of self-centering damage-free connections for seismic-resilient steel moment resisting frames. *Earthquake Engng Struct Dyn*. 2022;51(5):1292-1316. doi:10.1002/eqe.3615
31. Pieroni L, Di Benedetto S, Freddi F, Latour M. Genetic algorithm for the optimal placement of Self-centering Damage-Free joints in steel MRFs. *J Constr Steel Res*. 2022;197:107489. doi:10.1016/j.jcsr.2022.107489
32. Inamas H, u, Kanvinde AM, Lignos DG. Seismic design of non-dissipative embedded column base connections. *J Const Steel Res*. 2021;177:106417. doi:10.1016/j.jcsr.2020.106417

33. Cui Y, Nakashima M. Hysteretic behavior and strength capacity of shallowly embedded steel column bases. *J Struct Eng*. 2009;135(10):1231-1238. doi:10.1061/(ASCE)ST.1943-541X.0000056
34. Yu-Feng A, Lin-Hai H. Behavior of concrete-encased CFST columns under combined compression and bending. *J Constr Steel Res*. 2014;101:314-330. doi:10.1016/j.jcsr.2014.06.002
35. Latour M, Rizzano G. A theoretical model for predicting the rotational capacity of steel base joints. *Eng Struct*. 2013;91:89-99. https://doi.org/10.1016/j.jcsr.2013.08.009
36. Rodas PT, Zareian F, Kanvinde A. Hysteretic model for exposed column-base connections. *J Struct Eng*. 2016;142(12):1-14. doi:10.1061/(ASCE)ST.1943-541X.0001602
37. Elkady A, Lignos DG. Full-scale Testing of deep wide-flange steel columns under multi-axis cyclic loading: loading sequence, boundary effects, and lateral stability bracing force demands. *J Struct Eng*. 2018;144(2):04017189. doi:10.1061/(ASCE)ST.1943-541X.0001937
38. Elkady A, Güell G. Lignos Dimitrios G. Proposed methodology for building-specific earthquake loss assessment including column residual axial shortening. *Earthquake Engng Struct Dyn*. 2020;49:339-355. doi:10.1002/eqe.3242H
39. Inamasu H, Lignos DG. Seismic performance of steel columns interacting with embedded column bases while exhibiting inelastic deformations. *Eng Struct*. 2022;251:113381. doi:10.1016/j.engstruct.2021.113381
40. MacRae GA, Urmson CR, Walpole WR, Moss P, Hyde K, Clifton GC. Axial shortening of steel columns in buildings subjected to earthquakes. *Bulletin New Zealand Soc Earthq Eng*. 2009;42(4):275-287. doi:10.5459/bnzsee.42.4.275-287
41. Borzouie J, Macrae G, Chase JG, Rodgers GW, Clifton GC. Experimental studies on cyclic performance of CB strong axis–aligned asymmetric friction connections. *J Struct Eng (ASCE)*. 2016;142(1):1-10. doi:10.1061/(ASCE)ST.1943-541X.0001327
42. Freddi F, Dimopoulos CA, Karavasilis TL. Rocking damage-free steel CB with friction devices: design procedure and numerical evaluation. *Earthquake Engng Struct Dyn*. 2017;46(14):2281-2300. doi:10.1002/eqe.2904
43. Freddi F, Dimopoulos CA, Karavasilis TL. Experimental evaluation of a rocking damage-free steel CB with friction devices. *J Struct Eng*. 2020;146(10):1-20. doi:10.1061/(ASCE)ST.1943-541X.0002779 0402021
44. Kamperidis VC, Karavasilis TL, Vasdravellis G. Self-centering steel CB with metallic energy dissipation devices. *J Constr Steel Res*. 2018;149:14-30. doi:10.1016/j.jcsr.2018.06.027
45. Wang XT, Xie CD, Lin LH, Li J. Seismic behavior of self-centering concrete-filled square steel tubular (CFST) CB. *J Constr Steel Res*. 2019;156:75-85. doi:10.1016/j.jcsr.2019.01.025
46. Wang B, Zhu S, Qui C-X, Jin H. High-performance self-centering steel columns with shape memory alloy bolts: design procedure and experimental evaluation. *Eng Struct*. 2019;182:446-458.
47. Inamasu H, de Castro e Sousa A, Güell G, Lignos DG. Anchor-yield exposed column bases for minimising residual deformations in seismic-resistant steel moment frames. *Earthquake Engng Struct Dyn*. 2021;50:1083-1100. doi:10.1002/eqe.3392H
48. Inamasu H, de Castro e Sousa A, Lignos DG. Development and experimental validation of dissipative embedded column base connections for enhanced seismic performance of steel moment-resisting frames. *J Struct Eng*. 2022;148(3):1-18. doi:10.1061/(ASCE)ST.1943-541X.0003259
49. Yan Z, Ramhormozian S, Clifton GC, et al. Numerical studies on the seismic response of a three-story low-damage steel framed structure incorporating seismic friction connections. *Resilient Cities Struct*. 2023;2(1):91-102. doi:10.1016/j.rcns.2023.02.007
50. Latour M, Rizzano G, Santiago A, Da Silva L. Experimental response of a low-yielding, self-centering, rocking CB joint with friction dampers. *Soil Dyn Earthq Eng*. 2019;116:580-592. doi:10.1016/j.soildyn.2018.10.011
51. Elettore E, Freddi F, Latour M, Rizzano G. Design and analysis of a seismic resilient steel moment-resisting frame equipped with damage-free self-centering CBs. *J Constr Steel Res*. 2021;179:106543. doi:10.1016/j.jcsr.2021.106543
52. Elettore E, Lettieri A, Freddi F, Latour M, Rizzano G. Performance-based assessment of seismic-resilient steel moment resisting frames equipped with innovative column base connections. *Structures*. 2021;32:1646-1664.
53. Lettieri A, Elettore E, Pieroni L, Freddi F, Latour M, Rizzano G. Parametric analysis of steel MRFs with self-centering column bases. *Steel Constr*. 2022;15(2):91-99. doi:10.1002/stco.202100050
54. Elettore E, Freddi F, Latour M, Rizzano G. Parametric finite element analysis of self-centering column bases with different structural properties. *J Constr Steel Res*. 2022;199:107628. doi:10.1016/j.jcsr.2022.107628
55. Di Benedetto S, Francavilla AB, Latour M, Piluso V, Rizzano G. Pseudo-dynamic Testing of a full-scale two-story steel building with RBS connections. *Eng Struct*. 2020;212:110494. doi:10.1016/j.engstruct.2020.110494
56. Shegay AV, Miura K, Akira M, Maeda M, Seki M. Performance recovery of a repaired 4-story reinforced concrete structure subjected to shake-table Testing. *Earthquake Engng Struct Dyn*. 2023:1-21.
57. Zhang R, Xie J-H, Chouery KE, et al. Strong axis low-damage performance of rocking column-base joints with asymmetric friction connections. *Journ Constr Steel Res*. 2022;191:107175. doi:10.1016/j.jcsr.2022.107175
58. Mahin SA, Shing PB. Pseudo-dynamic method for seismic Testing. *J Struct Eng*. 1985;111:1482-1503. doi:10.1061/(ASCE)0733-9445(1985)111:7(1482)
59. Bruneau M, Chang SE, Eguchi RT, et al. A framework to quantitatively assess and enhance the seismic resilience of communities. *Earthquake Spectra*. 2003;19(4):733-752. doi:10.1193/1.1623497
60. Terzic V, Villanueva PK, Saldana D, Yoo DY. Framework for modelling post-earthquake functional recovery of buildings. *Eng Struct*. 2021;246:113074. doi:10.1016/j.engstruct.2021.113074
61. Earthquake Engineering Research Institute (EERI), Functional Recovery: A Conceptual Framework with Policy Options; 2019

62. Mazzoni S, McKenna F, Scott MH, Fenves GL. OpenSees: Open System for earthquake engineering simulation. *Pacific Earthquake Engineering Research Centre (PEER)*. University of California; 2009. http://opensees.berkeley.edu. Available at.
63. Vamvatsikos D, Cornell CA. Incremental dynamic analysis. *Earthquake Engng Struct Dyn*. 2002;31(3):491-514.
64. EN 1993-1-8. *Eurocode 3: Design of steel structures, Part 1–8: Design of steel structure: General rules and rules for buildings*, European Committee for Standardization, 2005
65. prEN 1998-1-2:2022, Eurocode 8: Earthquake resistance design of structures, draft
66. EN ISO 6892-1. *Metallic materials—Tensile Testing—Part 1: Method of Test at room temperature*. European Committee for Standardization. 2009.
67. EN 1090–2. Execution of steel structure and aluminium structure: technical requirements for steel structures.
68. EN 15129. Anti-seismic devices
69. Shen Y, Freddi F, Li Y, Li J. Parametric experimental investigation of unbonded post-tensioned reinforced concrete bridge piers under cyclic loading. *Earthquake Engng Struct Dyn*. 2022;51(15):3479-3504.
70. DIN 67-26 2006, Technical delivery conditions for fasteners—Part 26: Conical spring washers for bolt/nut assemblies
71. Ramhormozian S, Clifton GC, MacRae GA, Davet GP. Stiffness-based approach for Belleville springs use in friction sliding structural connections. *J Constr Steel Res*. 2017;138:340-356. doi:10.1016/j.jcsr.2017.07.009
72. Model 493.10/793.00 Controller Service. Minneapolis: MTS Systems Corp.; 2002.
73. SIMQKE-1 (SIMulation of earthQuaKE ground motions) http://nisee.berkeley.edu/software/simqke1/
74. Iervolino I, Galasso C, Cosenza E. REXEL: computer aided record selection for code-based seismic structural analysis. *B Earthq Eng*. 2010;8:339-362.

How to cite this article: Elettore E, Freddi F, Latour M, Piluso V, Rizzano G. Pseudo-dynamic testing, repairability, and resilience assessment of a large-scale steel structure equipped with self-centering column bases. *Earthquake Engng Struct Dyn*. 2024;53:2756–2781. https://doi.org/10.1002/eqe.4131